Philosophical Magazine,
Vol. 85, No. 1, 1 January 2005, 79–113

Taylor & Francis
Taylor & Francis Group

The bridging scale for two-dimensional atomistic/continuum coupling

Harold S. Park†, Eduard G. Karpov†,
Wing Kam Liu† and Patrick A. Klein‡

†Department of Mechanical Engineering, Northwestern University,
Evanston, IL 60201, USA
‡Sandia National Laboratories, Livermore, CA 94551, USA

[*Received 16 2003 and accepted in revised form 15 July 2004*]

Abstract

In this paper, we present all necessary generalisations to extend the bridging scale, a finite-temperature multiple scale method which couples molecular dynamics (MD) and finite element (FE) simulations, to two dimensions. The crucial development is a numerical treatment of the boundary condition acting upon the reduced atomistic system, as such boundary conditions are analytically intractable beyond simple one-dimension systems. The approach presented in this paper offers distinct advantages compared to previous works, specifically the compact size of the resulting time history kernel, and the fact that the time history kernel can be calculated using an automated numerical procedure for arbitrary multi-dimensional lattice structures and interatomic potentials. We demonstrate the truly two-way nature of the coupled FE and reduced MD equations of motion via two example problems, wave propagation and dynamic crack propagation. Finally, we compare both problems to benchmark full MD simulations to validate the accuracy and efficiency of the proposed method.

§ 1. Introduction

During the last decade, thanks to a combination of exploding computational power and improved physical insight into material behaviour, continuum and atomistic simulations improved greatly. Both classes of methods are now used to solve problems which are more complicated than ever with greater accuracy than ever before. Nevertheless, there still exist problems for which neither method alone is sufficient. This is particularly true when faced with simulating structures and devices that are on the micro or nanoscale. In general, atomistic simulations cannot be used for such length scales due to the restrictions on the number of atoms that can be simulated, along with the time scales which they can be simulated for. In contrast, continuum simulations tend to fail at the atomic scale, for example due to the inability of continuum models to describe defects. It is precisely at these length scales where multi-scale simulation methods, or those which strive to combine the

† Author for correspondence. Email: w-liu@northwestern.edu

Philosophical Magazine ISSN 1478–6435 print/ISSN 1478–6443 online
http://www.tandf.co.uk/journals
DOI: 10.1080/14786430412331300163

salient points of simulations which typically succeed at single length scales, are needed.

The best known multiple scale methods include the macroscopic, atomistic, *ab initio* dynamics (MAAD) method of Abraham *et al.* (1998), and the quasi-continuum (QC) method of Tadmor *et al.* (1996). MAAD was demonstrated on the dynamic fracture of silicon, while the QC was validated on quasi-static problems such as nano-indentation. Recently developed works include the bridging domain method of Xiao and Belytschko (2004), and the coupled atomistic dislocation dynamics (CADD) method of Shilkrot *et al.* (2004). As the present work is not intended as an exhaustive review, we refer the interested reader to two recent review papers on multiple scale methods, those of Liu *et al.* (2004), and Curtin and Miller (2003).

Recently, an alternative multi-scale approach, the bridging scale, was developed by Wagner and Liu (2003) to couple MD and FE. In the bridging scale, the continuum representation exists *everywhere* in the domain, including those areas in which MD is present. By using a projection operator to decompose the displacement field into orthogonal coarse and fine scales, they were able to derive a coupled set of equations of motion describing the evolution of the MD and FE systems. These coupled but separate equations of motion have three major benefits. The first is that, unlike MAAD, the FE and MD equations of motion are not required to be integrated using the same time step. The second benefit is that it allows the elimination of unwanted MD degrees of freedom by accounting for them in the form of an impedance force which augments the standard MD equations of motion. Because the unwanted MD degrees of freedom are accounted for in a consistent manner, high-frequency waves which cannot be represented by the continuum mesh are dissipated naturally out of the MD region. Lastly, unlike the QC method, the bridging scale is valid for finite-temperature dynamic problems.

The major contribution of this work is an extension of the analytically derived multiple scale molecular dynamics boundary condition in the Wagner and Liu (2003) work such that it can be calculated numerically in higher dimensions. Karpov *et al.* (2005) demonstrated these conditions within single scale settings. This development is a key step in the usage of such multiple scale methods, as analytic solutions for the boundary condition have proven to be intractable above one dimension. As a result of the derivation, a time history kernel similar in concept to the damping kernels previously derived analytically by Adelman and Doll (1976) in one-dimension, and numerically by Cai *et al.* (2000) and E and Huang (2002) in multiple dimensions is obtained. As will be demonstrated, the time history kernel derived in this work offers distinct advantages to previous work; specifically, the salient features are the compact size of the time history kernel matrix, and the fact that the time history kernel can be computed using an automated numerical procedure which involves only standard Laplace and Fourier transform techniques.

The layout of this paper is as follows. We first briefly review the bridging scale fundamentals, and derive the coupled FE and MD equations of motion. We motivate the need to eliminate the MD region from large parts of the domain and demonstrate how the eliminated fine scale degrees of freedom are accounted for in the numerically calculated time history kernel. As a result, a truly two-way boundary condition is established on the MD region, which both accounts for the eliminated fine scale degrees of freedom and is coupled to the overlaying coarse scale. We apply the bridging scale to two two-dimensional examples: wave propagation and dynamic crack propagation. Concluding remarks address further research possibilities using the bridging scale.

§ 2. Overview of bridging scale

2.1. *Bridging scale fundamentals*

The bridging scale was recently developed by Wagner and Liu (2003) to concurrently couple atomistic and continuum simulations. This bridging scale approach was first used by Liu *et al*. (1997) to enrich the finite element method with meshfree shape functions. Wagner and Liu (2001) used this approach to consistently apply essential boundary conditions in meshfree simulations. Zhang *et al*. (2002) applied the bridging scale in fluid dynamics simulations, and Qian *et al*. (2004) recently used the bridging scale in quasi-static simulations of carbon nanotube buckling. The bridging scale was also used in conjunction with a multi-scale constitutive law to simulate strain localisation by Kadowaki and Liu (2004).

Because much of the following has already been derived (see Wagner and Liu (2003), Park and Liu (2004)), we refer the interested reader to those works for further details. The fundamental idea is to decompose the total displacement field $\mathbf{u}(\mathbf{x})$ into coarse and fine scales

$$\mathbf{u}(\mathbf{x}) = \bar{\mathbf{u}}(\mathbf{x}) + \mathbf{u}'(\mathbf{x}). \tag{1}$$

For consistency, Greek indices $(\alpha, \beta, \ldots)$ will define atoms for the remainder of this paper, and uppercase Roman indices $(I, J, \ldots)$ will define coarse scale nodes. The coarse scale is defined to be

$$\bar{\mathbf{u}}(\mathbf{X}_\alpha) = \sum_I N_I^\alpha \mathbf{d}_I. \tag{2}$$

Here, $N_I^\alpha = N_I(\mathbf{X}_\alpha)$ is the shape function of node I evaluated at the initial atomic position $\mathbf{X}_\alpha$, and $\mathbf{d}_I$ is the FE nodal displacement associated with node I.

The fine scale is defined to be the projection of the MD displacements $\mathbf{q}$ onto the FE basis functions subtracted from the total solution $\mathbf{u}$, which is equivalent to the MD displacements $\mathbf{q}$. In other words, the fine scale represents that part of the total solution that the coarse scale cannot represent,

$$\mathbf{u}' = \mathbf{q} - \mathbf{P}\mathbf{q}, \tag{3}$$

where the projection matrix $\mathbf{P}$ is defined to be

$$\mathbf{P} = \mathbf{N}\mathbf{M}^{-1}\mathbf{N}^{\mathrm{T}}\mathbf{M}_{\mathrm{A}}. \tag{4}$$

In (4), $\mathbf{M}_{\mathrm{A}}$ is a diagonal matrix with the atomic masses on the diagonal, $\mathbf{N}$ is a matrix containing the values of the FE shape functions evaluated at all the atomic positions and $\mathbf{M} = \mathbf{N}^{\mathrm{T}}\mathbf{M}_{\mathrm{A}}\mathbf{N}$ is the coarse scale mass matrix. In general, the size of $\mathbf{N}$ is $N_{a1} \times N_{n1}$, where N_{n1} is the number of finite element nodes whose support contains an atomic position, and N_{a1} is the total number of atoms. We note that $\mathbf{P}$ satisfies the definition of a projection matrix, i.e. $\mathbf{P}\mathbf{P} = \mathbf{P}$. The total displacement $\mathbf{u}$ can finally be written as the sum of the coarse and fine scales as

$$\mathbf{u} = \mathbf{N}\mathbf{d} + \mathbf{q} - \mathbf{P}\mathbf{q}. \tag{5}$$

The final term in the above equation is called the bridging scale. It is the part of the solution that must be removed from the total displacement so that a complete separation of scales is achieved, i.e. the coarse and fine scales are orthogonal, or linearly independent of each other.

The coupled MD and FE equations of motion are derived using (5) by first constructing a multi-scale Lagrangian $\mathcal{L}$, which is defined to be the kinetic energy minus the potential energy

$$\mathcal{L}(\mathbf{u}, \dot{\mathbf{u}}) = \mathcal{K}(\dot{\mathbf{u}}) - V(\mathbf{u}). \tag{6}$$

The multi-scale equations of motion are obtained from the Lagrangian by following the relations

$$\frac{\mathrm{d}}{\mathrm{d}t}\left(\frac{\partial L}{\partial \dot{\mathbf{d}}}\right) - \frac{\partial \mathcal{L}}{\partial \mathbf{d}} = 0, \tag{7}$$

$$\frac{\mathrm{d}}{\mathrm{d}t}\left(\frac{\partial \mathcal{L}}{\partial \dot{\mathbf{q}}}\right) - \frac{\partial \mathcal{L}}{\partial \mathbf{q}} = 0, \tag{8}$$

which give the coupled multi-scale equations of motion:

$$\mathbf{M}_{\mathrm{A}}\ddot{\mathbf{q}} = \mathbf{f}, \tag{9}$$

$$\mathbf{M}\ddot{\mathbf{d}} = \mathbf{N}^{\mathrm{T}}\mathbf{f}(\mathbf{u}). \tag{10}$$

Now that the coupled coarse and fine scale equations of motion have been derived, we make some brief comments:

(i) The fine scale equation (9) is simply the MD equation of motion. Therefore, a standard MD solver can be used to obtain the MD displacements $\mathbf{q}$, while the vector of total MD forces $\mathbf{f}$ can be found using any relevant potential energy function.

(ii) The coarse scale equation (10) is simply the FE equation of motion. Thus, we can use standard finite element methods to find the solution to (10), while noting that the finite element mass matrix $\mathbf{M}$ is defined to be a consistent mass matrix.

(iii) The coupling between the two equations is through the coarse scale internal force $\mathbf{N}^{\mathrm{T}}\mathbf{f}(\mathbf{u})$, which is a direct function of the MD internal force $\mathbf{f}$. In the region in which MD exists, the coarse scale force is calculated by extrapolating the MD internal force by way of the finite element shape functions $\mathbf{N}$. The MD internal forces can therefore be thought of as defining the constitutive relation for the finite element internal force.

(iv) The FE equation of motion is redundant for the case in which the MD and FE regions both exist everywhere in the domain, because the FE equation of motion is simply an approximation to the MD equation of motion, with the quality of the approximation governed by the finite element shape functions $\mathbf{N}$. We note that due to the Kronecker-delta property of the finite element shape functions, the coarse scale internal force $\mathbf{N}^{\mathrm{T}}\mathbf{f}(\mathbf{u})$ *exactly reduces* to the MD forces for the case in which the finite element nodes coexist with atomic positions. We shall remove this redundancy in the next section, when we create coupled MD/FE equations of motion for systems where the MD region is confined to a small portion of the domain.

(v) The total solution $\mathbf{u}$ satisfies the same equation of motion as $\mathbf{q}$, i.e.

$$\mathbf{M}_{\mathrm{A}}\ddot{\mathbf{u}} = \mathbf{f}. \tag{11}$$

This result is due to the fact that **q** and **u** satisfy the same initial conditions, and will be utilized in deriving the boundary conditions on the MD simulation in the following section.

2.2. *Removing fine scale degrees of freedom in the coarse scale only region*

2.2.1. *Linearized MD equation of motion at the boundary*

We imagine the bridging scale to be most applicable to problems in which the MD region is confined to a small portion of the domain, while the coarse scale representation exists everywhere. This coupled system is created by reducing the full system in which MD and FE exist everywhere in the domain; see figure 1 for an illustrative example. The single scale problem was solved analytically for some one-dimensional lattices by Adelman and Doll (1976), who used a harmonic approximation to eliminate the unwanted MD degrees of freedom. The equation of motion for the remaining atoms then has an additional term which takes the form of a time history integral involving the atomic velocities multiplied by a matrix $\boldsymbol{\beta}(t)$, known as the damping kernel. The damping kernel mimics the dissipation of fine scale energy into the eliminated degrees of freedom. However, the intractability of analytically deriving the damping kernel in multiple dimensions motivated methods to calculate the damping kernel numerically; numerical methods to calculate the damping matrix $\boldsymbol{\beta}(t)$, or equivalently its time derivative $\boldsymbol{\theta}(t)$, were proposed recently by Cai *et al.* (2000), and E and Huang (2002).

In this section, we present an approach such that the time history kernel matrix $\boldsymbol{\theta}(t)$ can be calculated numerically in multiple dimensions for the bridging scale method. The key idea is to utilize the periodicity of atomic structures so that the standard technique of discrete Fourier transforms can be applied (Karpov *et al.* 2002, 2003). Specifically, the method herein is similar to the works by Wagner *et al.* (2004), Karpov *et al.* (2005), Park *et al.* (2004a), which present methods to numerically calculate the damping kernel matrix in multiple dimensions for single

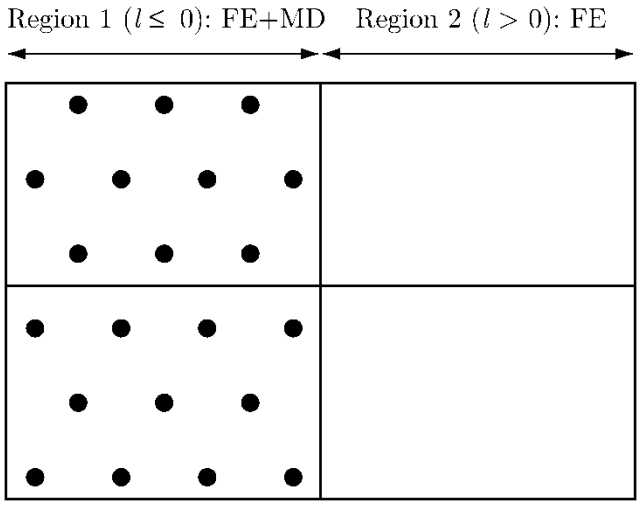

Figure 1. Separation of the problem into two regions. Region 1 is FE + reduced MD, region 2 is FE. This decomposition exists due to the elimination of the MD degrees of freedom in region 2.

scale, molecular dynamics simulations. Here, we generalize the approach such that it can be applied to multiple scale simulations.

In this approach, we assume that the atomistic region can be subdivided into two regions. In the first region, i.e. around a crack tip, defects or other locally interesting physical phenomena, an anharmonic, or nonlinear potential is necessary to accurately represent the atomic interactions. However, at some distance away from the process of interest, an anharmonic representation of the atomistic physics no longer becomes necessary. At this point, the atomic forces can be well represented as a linear function of the displacements, which implies small relative displacements and rotations of the lattice. Therefore, the remainder of this section will summarize the methodology used to eliminate those atoms which we assume to have harmonic-type behaviour while keeping their effects on the reduced MD system. We first partition the MD displacement degrees of freedom into harmonic and anharmonic components as

$$\mathbf{q} = \begin{pmatrix} \mathbf{q}_{\mathrm{a}} \\ \mathbf{q}_{\mathrm{h}} \end{pmatrix}, \tag{12}$$

where $\mathbf{q}_{\mathrm{a}}$ are the atomistic displacement degrees of freedom which behave anharmonically, and $\mathbf{q}_{\mathrm{h}}$ are the atomistic displacement degrees of freedom whose forces are linearly related to their displacements. It is important to recognize that the number of $\mathbf{q}_{\mathrm{a}}$ is small relative to the number of $\mathbf{q}_{\mathrm{h}}$, because the nonlinear representation is only necessary around the local physics of interest. More importantly, the number of $\mathbf{q}_{\mathrm{h}}$ is generally huge, and can be on the order of millions or billions of degrees of freedom. Because of the large number of these unnecessary degrees of freedom, we now demonstrate how to eliminate the $\mathbf{q}_{\mathrm{h}}$ degrees of freedom, while implicitly including their effects on the remaining, uneliminated nonlinear $\mathbf{q}_{\mathrm{a}}$ degrees of freedom. To do so, we first decompose (9) as

$$\mathbf{M}_{\mathrm{a}}\ddot{\mathbf{q}}_{\mathrm{a}} = \mathbf{f}(\mathbf{u}), \tag{13}$$

$$\mathbf{M}_{\mathrm{h}}\ddot{\mathbf{q}}_{\mathrm{h}} = \mathbf{f}(\mathbf{u}). \tag{14}$$

We next linearize the force $\mathbf{f}(\mathbf{u})$ in (14) about $\mathbf{u}' = 0$, and use the equality of $\mathbf{q}$ and $\mathbf{u}$ to rewrite (14) as

$$\mathbf{M}_{\mathrm{h}}\ddot{\bar{\mathbf{u}}}_{\mathrm{h}} + \mathbf{M}_{\mathrm{h}}\ddot{\mathbf{u}}'_{\mathrm{h}} = \mathbf{f}(\bar{\mathbf{u}}) + \mathbf{K}\mathbf{u}', \tag{15}$$

where the stiffness matrix $\mathbf{K}$ is defined as

$$\mathbf{K}_{\alpha\beta} = \frac{\partial \mathbf{f}_{\alpha}}{\partial \mathbf{u}_{\beta}}. \tag{16}$$

In (16), the subscript α includes all atoms in the domain, while the subscript β includes those atoms in region 2 that are to be eliminated, indicating that $\mathbf{K}_{\alpha\beta}$ is in general an extremely large matrix. Because the analytic calculation of $\boldsymbol{\theta}(t)$ requires a matrix inversion of $\mathbf{K}_{\alpha\beta}$ which is generally intractable, the next section details a procedure that utilizes the repetitive nature of $\mathbf{K}_{\alpha\beta}$ to calculate $\boldsymbol{\theta}(t)$ numerically. Note that no truncation or higher order terms results in (15) due to the fact that the linearisation was only performed on the harmonic portion of the MD region.

Because we wish to eliminate the fine scale from the majority of the domain while keeping the coarse scale everywhere, we assume the equating of coarse and fine scale components, and further decompose (15) into two equations as

$$\mathbf{M}_{\mathrm{h}}\ddot{\bar{\mathbf{u}}}_{\mathrm{h}} = \mathbf{f}(\bar{\mathbf{u}}), \tag{17}$$

$$\mathbf{M}_{\mathrm{h}}\ddot{\mathbf{u}}'_{\mathrm{h}} = \mathbf{K}\mathbf{u}'. \tag{18}$$

Continuing with the derivation, the fine scale equation (18) is rewritten as

$$\ddot{\mathbf{u}}'_{\mathrm{h}} = \mathbf{A}\mathbf{u}', \tag{19}$$

where $\mathbf{A} = \mathbf{M}_{\mathrm{h}}^{-1}\mathbf{K}$. Equation (19) is the major result of this section, and will be used as the basis for the next section, in which we will demonstrate how all of the harmonic fine scale degrees of freedom in (14) can be eliminated such that the nonlinear MD degrees of freedom defined by (13) exist only around the local physics of interest.

2.2.2. *Elimination of unnecessary harmonic fine scale segrees of freedom*

Because our stated goal is to entirely remove the harmonic portion of the fine scale region from the domain, we now utilize the periodicity of crystalline lattices to derive a numerical boundary condition on the fine scale region which will be recombined with the coarse scale equation (17) to lead to a non-reflecting MD boundary condition. The periodic lattice consists of spatially repeated unit cells which are repeated in two directions. Each repeated cell has n_{a} atoms, each of which can move in n_{SD} spatial directions. The total number of degrees of freedom in each unit cell is then $n_{\mathrm{dof}} = n_{\mathrm{a}} \times n_{\mathrm{SD}}$. Each unit cell can be labelled with two indices, l and m, indicating the position along axes in the direction of the two (in two dimensions) primitive vectors of the crystal structure. This is illustrated in figure 2. Equation (19) can thus be re-written as

$$\ddot{\mathbf{u}}'_{l,m}(t) = \sum_{l'=l-1}^{l+1} \sum_{m'=m-\mu}^{m+\mu} \mathbf{M}_{\mathrm{h}}^{-1}\mathbf{K}_{l-l',m-m'}\mathbf{u}'_{l',m'}(t) + \mathbf{M}_{\mathrm{h}}^{-1}\mathbf{f}^{\mathrm{ext}}_{l,m}(t), \tag{20}$$

where $\mathbf{f}^{\mathrm{ext}}_{l,m}(t)$ is the external force acting upon unit cell (l,m), the constant matrices $\mathbf{K}$ relate the displacements in cell $(-l', -m')$ to the forces in cell (l,m) and μ represents the range of the forces in the m coordinate direction. We note that while atoms in a given slab of constant l are coupled to only neighbouring cells $l-1$ and $l+1$, the coupling in the m coordinate direction is not limited to nearest neighbours. Further comments on $\mathbf{K}$ for a specific interatomic potential are given in appendix A.

Equation (20) is valid for any unit cell within the harmonic fine scale region, and indicates that each atom comprises a unit cell with two degrees of freedom (due to the two-dimensional problems we are considering). The summation then indicates that each atom interacts only with its nearest neighbours; this approximation can be relaxed simply by increasing the size of the unit cell if longer ranged interactions are desired, and is the focus of current work (Park *et al.* 2004b).

The next step is to transform (20) by taking a Laplace transform (LT) and a discrete Fourier transform (DFT), giving

$$s^2\hat{\mathbf{U}}'(p,q,s) - s\mathbf{u}'(p,q,0) - \dot{\mathbf{u}}'(p,q,0) = \hat{\mathbf{A}}(p,q)\hat{\mathbf{U}}'(p,q,s) + \mathbf{M}_{\mathrm{h}}^{-1}\hat{\mathbf{F}}_0^{\mathrm{ext}}(q,s), \tag{21}$$

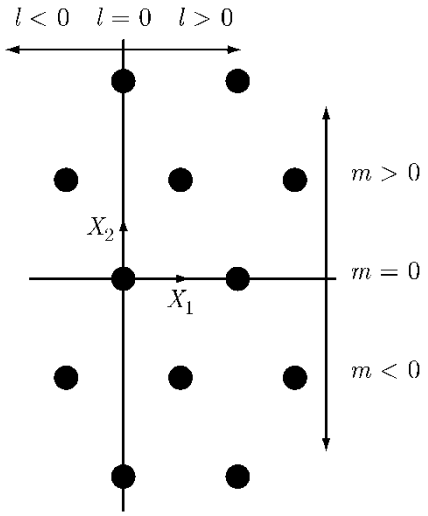

Figure 2. Graphical depiction of the lattice decomposed into that part which interacts anharmonically ($l < 0$), the boundary atoms ($l = 0$), and the harmonic portion which is mathematically eliminated ($l > 0$).

where p and q correspond to spatial indices l and m, the hatted notation indicates the discrete Fourier transform, and Laplace transformed variables are indicated by the transformed variable s. $\hat{\mathbf{A}}(p, q)$ is the Fourier transform of $\mathbf{M}_{\mathrm{h}}^{-1}\mathbf{K}_{l,m}$. Further details on the Laplace and Fourier transform techniques utilized in this section can be found in appendix A.

The goal of this process will be to eliminate the atoms in the $l > 0$ cells by solving for them in terms of the $l \leq 0$ degrees of freedom and resubstituting that expression into (20). In this manner, we will avoid the explicit solution for the $l > 0$ degrees of freedom while implicitly including their effects into the remaining system dynamics. We note that in taking the DFT of the stiffness matrices $\mathbf{K}$, it was assumed that the harmonic degrees of freedom $\mathbf{q}_{\mathrm{h}}$ are large enough and formally comprise a large, separate subdomain such that the DFT of only those degrees of freedom can be performed.

The key step in removing the unwanted $l > 0$ fine scale degrees of freedom is in realizing that the motion of the boundary ($l = 0$) atoms can be caused either by the displacements of the atoms to be kept, or by an external force acting upon the boundary atoms. Therefore, it will be assumed that the motion of the boundary atoms is in fact caused by the external force which acts only at $l = 0$

$$\mathbf{f}_{l,m}^{\mathrm{ext}}(t) = \delta_{l,0}\mathbf{f}_{0,m}^{\mathrm{ext}}(t). \tag{22}$$

Equation (21) can be solved to give the Laplace transformed/discrete Fourier transformed displacements in terms of the external force

$$\hat{\mathbf{U}}'(p, q, s) = \hat{\mathbf{G}}(p, q, s)(\mathbf{M}_{\mathrm{h}}^{-1}\hat{\mathbf{F}}_0^{\mathrm{ext}}(q, s) + s\mathbf{u}'(p, q, 0) + \dot{\mathbf{u}}'(p, q, 0)), \tag{23}$$

where

$$\hat{\mathbf{G}}(p, q, s) = (s^2\mathbf{I} - \hat{\mathbf{A}}(p, q))^{-1}. \tag{24}$$

Taking the inverse Fourier transform of (23) in the x direction gives the displacement in the x direction at atomic position l

$$\tilde{\mathbf{U}}'_l(q,s) = \tilde{\mathbf{G}}_l(q,s)\hat{\mathbf{F}}_0^{\text{ext}}(q,s) + s\sum_{l'}\tilde{\mathbf{G}}_{l-l'}(q,s)\mathbf{u}'_{l'}(q,0) + \sum_{l'}\tilde{\mathbf{G}}_{l-l'}(q,s)\dot{\mathbf{u}}'_{l'}(q,0). \tag{25}$$

We use the tilde notation to denote mixed space–wavenumber functions, i.e. functions of space in the x direction (through index l), and wavenumber in the y direction (through q). By writing (25) for both $l=0$ and $l=1$, we can obtain the displacements $\tilde{\mathbf{U}}'_1$ in terms of $\tilde{\mathbf{U}}'_0$, thereby eliminating $\hat{\mathbf{F}}_0^{\text{ext}}$ and obtaining

$$\begin{aligned}\tilde{\mathbf{U}}'_1(q,s) = \tilde{\mathbf{G}}_1(q,s)\tilde{\mathbf{G}}_0^{-1}(q,s)\tilde{\mathbf{U}}'_0(q,s) + s\sum_{l'}\tilde{\mathbf{G}}_{l-l'}(q,s)\mathbf{u}'_{l'}(q,0)\\ + \sum_{l'}\tilde{\mathbf{G}}_{l-l'}(q,s)\dot{\mathbf{u}}'_{l'}(q,0).\end{aligned} \tag{26}$$

By inverting the Fourier transform and using the convolution property of the DFT, we get

$$\mathbf{U}'_{1,m}(s) = \sum_{m'=-M/2+1}^{M/2}\mathbf{Q}_{m-m'}(s)(\mathbf{U}'_{0,m'}(s) - \mathbf{R}_{0,m'}(s)) + \mathbf{R}_{1,m}(s), \tag{27}$$

where

$$\tilde{\mathbf{Q}}(q,s) = \tilde{\mathbf{G}}_1(q,s)\tilde{\mathbf{G}}_0^{-1}(q,s) \tag{28}$$

and

$$\begin{aligned}\mathbf{R}_{l,m}(s) = s\sum_{l'}\sum_{m'=-M/2+1}^{M/2}\tilde{\mathbf{G}}_{l-l',m-m'}(s)\mathbf{u}'_{l',m'}(0)\\ + \sum_{l'}\sum_{m'=-M/2+1}^{M/2}\tilde{\mathbf{G}}_{l-l',m-m'}(s)\dot{\mathbf{u}}'_{l',m'}(0).\end{aligned} \tag{29}$$

Equation (27) becomes useful when it is recalled that the linearized forces acting on slab $l=0$ due to slab $l=1$ can be written as, recalling (20)

$$\mathbf{F}_m^{1\to 0}(s) = \sum_{m'=m-\mu}^{m+\mu}\mathbf{K}_{-1,m-m'}\mathbf{U}'_{1,m'}(s). \tag{30}$$

Substituting (27) into (30) and taking the inverse Laplace transform, the force boundary condition of the slab $l=1$ atoms acting upon the slab $l=0$ atoms becomes

$$\mathbf{f}_m^{1\to 0}(t) = \sum_{m'=-M/2+1}^{M/2}\int_0^t \boldsymbol{\theta}_{m-m'}(t-\tau)(\mathbf{u}'_{0,m'}(\tau) - \mathbf{R}_{0,m'}(\tau))\,\mathrm{d}\tau + \mathbf{R}^{\text{f}}_{0,m}(t), \tag{31}$$

where the time history kernel $\boldsymbol{\theta}_m(t)$ is defined to be

$$\boldsymbol{\theta}_m(t) = \mathcal{L}^{-1}(\boldsymbol{\Theta}_m(s)) \tag{32}$$

and

$$\mathbf{\Theta}_{m-m'}(s) = \sum_{m'=m-\mu}^{m+\mu} \mathbf{K}_{-1,\,m-m'}\mathbf{Q}_{m'}(s). \tag{33}$$

The random displacement $\mathbf{R}_{l,\,m}(t)$ is defined to be

$$\mathbf{R}_{l,\,m}(t) = \sum_{l'} \sum_{m'=-M/2+1}^{M/2} \dot{\mathbf{g}}_{l-l',\,m-m'}(t)\mathbf{u}'_{l',\,m'}(0) + \sum_{l'} \sum_{m'=-M/2+1}^{M/2} \mathbf{g}_{l-l',\,m-m'}(t)\dot{\mathbf{u}}'_{l',\,m'}(0), \tag{34}$$

where

$$\mathbf{g}_{l-l',\,m-m'}(t) = \mathcal{F}^{-1}\mathcal{L}^{-1}(\tilde{\mathbf{G}}(q,s)), \tag{35}$$

$$\dot{\mathbf{g}}_{l-l',\,m-m'}(t) = \mathcal{F}^{-1}\mathcal{L}^{-1}(s\tilde{\mathbf{G}}(s)) = \mathcal{F}^{-1}\mathcal{L}^{-1}(s\tilde{\mathbf{G}}(s) - \mathbf{g}(0)), \tag{36}$$

and $\mathbf{u}'(0)$, $\dot{\mathbf{u}}'(0)$ are random initial displacements and velocities that can be sampled based on the Maxwell–Boltzmann distribution. The random force $\mathbf{R}^{\mathrm{f}}_{0,\,m}(t)$ in (33) is defined to be

$$\mathbf{R}^{\mathrm{f}}_{0,\,m}(t) = \sum_{m'=-M/2+1}^{M/2} \mathbf{K}_{-1,\,m-m'}\mathbf{R}_{1,\,m'}(t). \tag{37}$$

The fine scale equation of motion (19) for the boundary $l=0$ atoms can now be rewritten as

$$\ddot{\mathbf{u}}'_{0,\,m} = \mathbf{A}_{0,\,m}\mathbf{u}'_{0,\,m} + \mathbf{M}_{\mathrm{h}}^{-1}\left(\sum_{m'=-M/2+1}^{M/2} \int_0^t \boldsymbol{\theta}_{m-m'}(t-\tau)(\mathbf{u}'_{0,\,m'}(\tau) - \mathbf{R}_{0,\,m'}(\tau))\,\mathrm{d}\tau + \mathbf{R}^{\mathrm{f}}_{0,\,m}(t) \right). \tag{38}$$

Note that the second term on the right-hand side of (38) represents the implicit effects of the $l > 0$ cells which were eliminated from the system. Adding (38) and (17) and noting that

$$\mathbf{M}_{\mathrm{h}}^{-1}\mathbf{f}_{0,\,m}(\bar{\mathbf{u}}) + \mathbf{A}_{l,\,m}\mathbf{u}'_{0,\,m}(t) = \mathbf{M}_{\mathrm{h0}}^{-1}\mathbf{f}_{0,\,m}(\bar{\mathbf{u}}, \mathbf{u}'_{\mathrm{a}}, \mathbf{u}'_{\mathrm{h}} = 0), \tag{39}$$

where $\mathbf{M}_{\mathrm{h0}}$ is a diagonal matrix containing the masses of the boundary ($l = 0$) atoms, we obtain the modified equation of motion for the boundary atoms which does not involve any unknown degrees of freedom of the cells (l, m) with $l > 0$

$$\mathbf{M}_{\mathrm{h0}}\ddot{\mathbf{q}}_{0,\,m}(t) = \mathbf{f}_{0,\,m}(\bar{\mathbf{u}}, \mathbf{u}'_{\mathrm{a}}, \mathbf{u}'_{\mathrm{h}} = 0) + \sum_{m'=M/2+1}^{M/2} \int_0^t \boldsymbol{\theta}_{m-m'}(t-\tau)\big(\mathbf{u}'_{0,\,m'}(\tau) - \mathbf{R}_{0,\,m'}(\tau)\big)\,\mathrm{d}\tau + \mathbf{R}^{\mathrm{f}}_{0,\,m}(t). \tag{40}$$

As can be seen, the exact evaluation of the second term on the right-hand side of (40) requires a summation over all other unit cells along the boundary. Clearly,

it would be computationally inefficient to actually perform the exact summation in practice, particularly if the lattice is large. Therefore, we rewrite (40) as

$$\mathbf{M}_{\mathrm{h}0}\ddot{\mathbf{q}}_{0,m}(t) = \mathbf{f}_{0,m}(\bar{\mathbf{u}}, \mathbf{u}'_{\mathrm{a}}, \mathbf{u}'_{\mathrm{h}} = 0) + \sum_{m'=m-n_{\mathrm{crit}}}^{m+n_{\mathrm{crit}}} \int_0^t \boldsymbol{\theta}_{m-m'}(t-\tau)(\mathbf{u}'_{0,m'}(\tau) - \mathbf{R}_{0,m'}(\tau))\,\mathrm{d}\tau + \mathbf{R}^{\mathrm{f}}_{0,m}(t), \quad (41)$$

where n_{crit} refers to a maximum number of atomic neighbours which will be used to compute the impedance force. The final step to writing the MD equations of motion for the boundary atoms is to note that the fine scale component of the MD displacements can be written as

$$\mathbf{u}'_{0,m'}(\tau) = \mathbf{q}_{0,m'}(\tau) - \bar{\mathbf{u}}_{0,m'}(\tau). \quad (42)$$

The final form for the coupled MD and FE equations of motion thus can be written as

$$\mathbf{M}_{\mathrm{a}}\ddot{\mathbf{q}}_{\mathrm{a}} = \mathbf{f}(\bar{\mathbf{u}}, \mathbf{u}'_{\mathrm{a}}, \mathbf{u}'_{\mathrm{h}} = 0), \quad (43)$$

$$\mathbf{M}_{\mathrm{h}0}\ddot{\mathbf{q}}_{0,m}(t) = \mathbf{f}_{0,m}(t) + \mathbf{f}^{\mathrm{imp}}_{0,m}(t) + \mathbf{R}^{\mathrm{f}}_{0,m}(t), \quad (44)$$

$$\mathbf{f}^{\mathrm{imp}}_{0,m}(t) = \sum_{m'=-n_{\mathrm{crit}}}^{n_{\mathrm{crit}}} \int_0^t \boldsymbol{\theta}_{m-m'}(t-\tau)(\mathbf{q}_{0,m'}(\tau) - \bar{\mathbf{u}}_{0,m'}(\tau) - \mathbf{R}_{0,m'}(\tau))\,\mathrm{d}\tau, \quad (45)$$

$$\mathbf{M}\ddot{\mathbf{d}} = \mathbf{N}^{\mathrm{T}}\mathbf{f}(\mathbf{u}). \quad (46)$$

Equations (43)–(46) represent the major results of this section. With these key equations having been derived, several remarks are in order:

(i) The first equation (43) defines the standard MD equation of motion, with interatomic forces derived from any anharmonic potential energy function. This equation is solved for all non-boundary atoms.

(ii) The second equation (44) is the modified MD equation of motion for the boundary atoms. The first term on the right-hand side of (44), $\mathbf{f}_{0,m}(t)$, is simply the interatomic force calculated assuming that the fine scale for the $l > 0$ cells is zero. In other words, this is just the standard nonlinear interatomic force that is calculated in the MD simulation. It is important to note that this force is the standard nonlinear interatomic force; the assumption of linearity was only used in describing the motion of the $l > 0$ cells which were eliminated. Specifically, the assumption of linearity manifests itself in the time history kernel $\boldsymbol{\theta}(t-\tau)$.

(iii) For clarity of explanation, we have shown (43) and (44) as separate equations. In practice, no separate MD equation of motion is solved for only the boundary $l = 0$ atoms. Instead, the impedance force $\mathbf{f}^{\mathrm{imp}}_{0,m}(t)$ in (44) and the stochastic force $\mathbf{R}_{0,m}(t)$ can simply be added to the right-hand side of the MD equation of motion as external forces acting *only* on the MD boundary atoms. In this way, no additional equations to solve are introduced.

(iv) The second term on the right-hand side of (44), the impedance force $\mathbf{f}^{\mathrm{imp}}_{0,m}(t)$, contains the time history kernel $\boldsymbol{\theta}(t-\tau)$, and acts to dissipate fine scale energy from the MD simulation into the surrounding continuum.

In comparing this term to the previously derived one-dimensional boundary condition of Wagner and Liu (2003), the major difference is that the time history kernel $\boldsymbol{\theta}(t-\tau)$ is now computed numerically instead of analytically, as was done for the one-dimensional case. The result is a non-reflecting boundary between the MD and FE regions, as the time history kernel allows short wavelengths that cannot be represented by the surrounding continuum to leave the MD region.

(v) The random displacement $\mathbf{R}_{0,m'}(\tau)$ in (45) and the random force $\mathbf{R}^{\mathrm{f}}_{0,m}(t)$ in (44) act on the reduced atomistic system due to initial conditions in the continuum region. Because the initial conditions can be known only in an averaged sense based on the temperature of the coarse scale, and because many different initial conditions are possible, the random terms represent thermally dependent excitations exerted on the MD region by the surrounding coarse scale. The existence of these random terms indicates that the bridging scale method can be considered a coupled finite-temperature method; techniques for applying these stochastic terms were proposed by Adelman and Doll (1976). In the examples presented in this paper, we neglect this random term, indicating that the temperature of the surrounding continuum is 0 K.

(vi) We note that the time history kernel $\boldsymbol{\theta}(t)$ is a 2×2 matrix, corresponding to the minimum number of degrees of freedom in each unit cell. The compact size of $\boldsymbol{\theta}(t)$ distinguishes this approach from other methods, such as that of Cai *et al.* (2000), and E and Huang (2002). These differences will be elaborated in the next section. The small size of $\boldsymbol{\theta}(t)$ enables us to achieve large computational savings by eliminating large portions of the lattice where an explicit atomistic representation is not desired. Specifically, even as the number of eliminated $\mathbf{q}_{\mathrm{h}}$ harmonic fine scale degrees of freedom grows, the size of $\boldsymbol{\theta}(t)$ remains constant.

(vii) Due to the elimination of the fine scale degrees of freedom for the $l > 0$ cells, the FE equation of motion (46) is *not redundant*. The coarse scale thus carries two major responsibilities. The first is to capture the long wavelength nonlinear response of the system, while the impedance force $\mathbf{f}^{\mathrm{imp}}_{0,m}(t)$ described in remark (iv) accounts for the high-frequency waves that cannot be captured by the coarse scale. The second major role of the coarse scale relates to the coupling of the revised MD equation of motion (44) such that it depends upon the coarse scale solution $\bar{\mathbf{u}}_{0,m'}(\tau)$ through the impedance force $\mathbf{f}^{\mathrm{imp}}_{0,m}(t)$ in (45). The coarse scale dependence in (44) then serves as a boundary condition on the MD simulation, should the flow of information be from continuum to atomistic regions. In this manner, a true two-way coupling between the coarse and fine scales has been achieved.

(viii) For the coupled system of equations describing a domain in which FEM and MD both exist everywhere, i.e. (9) and (10), the global system is conservative. However, due to the elimination of the $\mathbf{q}_{\mathrm{h}}$ harmonic fine scale degrees of freedom, the MD system described by (43) and (44) is dissipative.

(ix) Due to the fact that the bridging scale involves the solution of the standard FE and MD equations of motion with few modifications, the method is extremely well suited to the reusage of existing FE and MD codes. The changes to the standard MD equation of motion, as previously

mentioned in remarks (iv) and (v), only involves the additional impedance and random forces applied to the boundary atoms. For the FE equation of motion, the FE internal forces are computed using the MD forces as a function of the total displacement $\mathbf{u}$; therefore, the subroutine used to calculate the actual MD forces can simply be reused to calculate the FE internal force $\mathbf{N}^{\mathrm{T}}(\mathbf{u})$.

(x) The motion of the ghost atoms, which exist such that the reduced atomistic system does not see a surface, is controlled using the finite element shape functions. This procedure is identical to that adopted to control the motion of the pad, or ghost atoms in Shilkrot *et al.* (2004). We note that the ghost-atom displacements can be calculated directly by taking the inverse Laplace transform of (27), and adding on the coarse scale component of the displacement. However, previous works by Adelman and Doll (1976), Cai *et al.* (2000), and E and Huang (2002) have utilized a force boundary condition. Therefore, we follow convention and use the impedance force formulation while controlling the motion of the ghost atoms using the finite element shape functions.

2.3. *Comparison of time history kernel to previous methods*

The time history kernel matrix $\boldsymbol{\theta}(t)$ derived in the previous section bears much resemblance to other non-reflecting boundary conditions derived by Adelman and Doll (1976), Cai *et al.* (2000), and E and Huang (2002). All methods have been shown to eliminate high-frequency wave reflection at the MD/FE interface by the derivation and utilization of either $\boldsymbol{\beta}(t)$, which is known as the damping kernel, or its time derivative $\boldsymbol{\theta}(t)$. As the methodology of Adelman and Doll was limited to one-dimensional examples, we compare our approach to the other two methods mentioned above.

The work of Cai *et al.* (2000) is a seminal one due to the fact that it was one of the first works to numerically calculate the damping kernel $\boldsymbol{\beta}(t)$ in multiple dimensions. However, the work contains two potential drawbacks. Firstly, the damping kernel of Cai requires multiple MD simulations on a larger domain to obtain. Secondly, the size of the damping kernel is proportional to N, with N being the total number of degrees of freedom in the reduced MD domain.

The work of E and Huang (2002) was based on removing wave reflection at the MD boundary by optimizing the reflection coefficient at the boundary. Because of this, multiple MD simulations were not required to obtain the damping kernel. The formulation of E and Huang, however, introduces other difficulties. First of all, the geometry of the lattice enters their formulation explicitly, and must be accounted for in each calculation of the time history kernel. Secondly, the angles of incidence of waves approaching the interface also need to be specified; it is unclear if the formulation allows waves impinging on the boundary at arbitrary angles within a single calculation.

The work presented herein remedies the above difficulties as follows. First, and most importantly, the size of $\boldsymbol{\theta}(t)$ is that of the minimum number of degrees of freedom in each unit cell. For example, in the current two-dimensional formulation, $\boldsymbol{\theta}(t)$ is a 2×2 matrix. Secondly, the geometry of the lattice need not be explicitly modeled; the effects are contained in the $\mathbf{K}$ matrices that can easily be derived for arbitrary lattice geometries and interatomic potentials. Thirdly,

due to the repetitive structure of the atomic lattice, the same $\boldsymbol{\theta}(t)$ is used for each boundary atom in the numerical implementation. Finally, as demonstrated in Wagner *et al.* (2004), and Karpov *et al.* (2005), the methodology for calculating $\boldsymbol{\theta}(t)$ numerically can be automated, and only requires standard Laplace and Fourier transform techniques, as well as the **K** matrices which define the interactions between an atom and all of its neighbours.

To complete the discussion regarding the methodology presented herein to numerically calculate the time history kernel $\boldsymbol{\theta}(t)$, we add the following comments:

(i) Because of the fact that the force on a given boundary atom includes the displacements of all of its neighbouring atoms (e.g. the sum in (45)), it is expected that this method will lose accuracy near lattice corners, where a full complement of atomic neighbours is generally unavailable.

(ii) It was assumed in deriving the MD impedance force (45) that the boundary layer of atomic unit cells (the $l=0$ slab in figure 2) is initially planar.

(iii) The formulation presented here is only used in this paper for cases in which the atoms in each unit cell interact with only the nearest-neighbour atoms. However, this is not a general restriction on the method. For longer ranged forces, simply increasing the size of the unit cell accounts for the additional interactions, and is the focus of work in progress (Park *et al.* 2004b).

(iv) The assumption of linearity is *only* required to hold for the atoms in the $l > 0$ unit cells which are eliminated from the formulation. Therefore, the method does not allow defects such as dislocations to propagate through the boundary. The remainder of the lattice is allowed to interact via any anharmonic potential desired.

(v) The four components of the time history kernel in (45) calculated for a hexagonal lattice interacting via a nearest-neighbour Lennard–Jones (LJ) 6–12 potential are shown in figures 3–6. As can be seen in the figures, the dominant order for each component is the zeroth-order ($n_{\text{crit}} = 0$), which corresponds to only taking the value of the displacements at each boundary atom, and not considering the displacements of any neighbouring atoms.

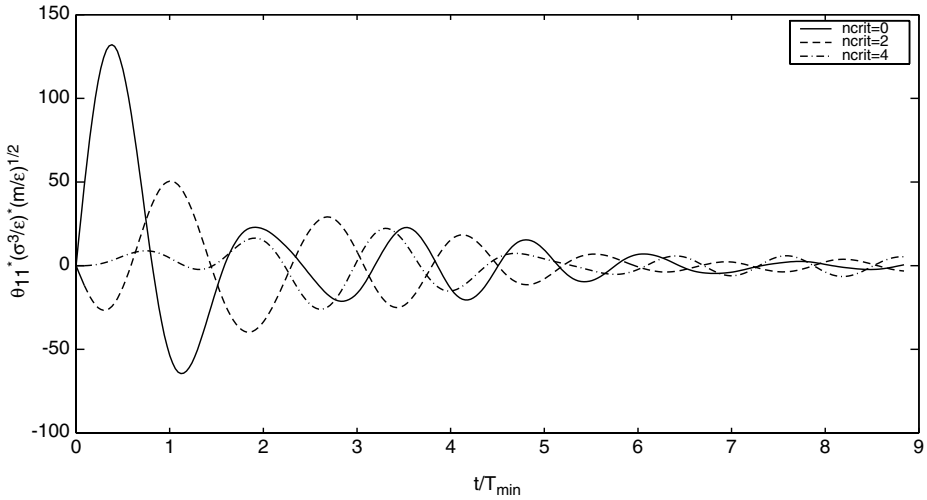

Figure 3. $\boldsymbol{\theta}_{11}(t)$ for zero and higher orders.

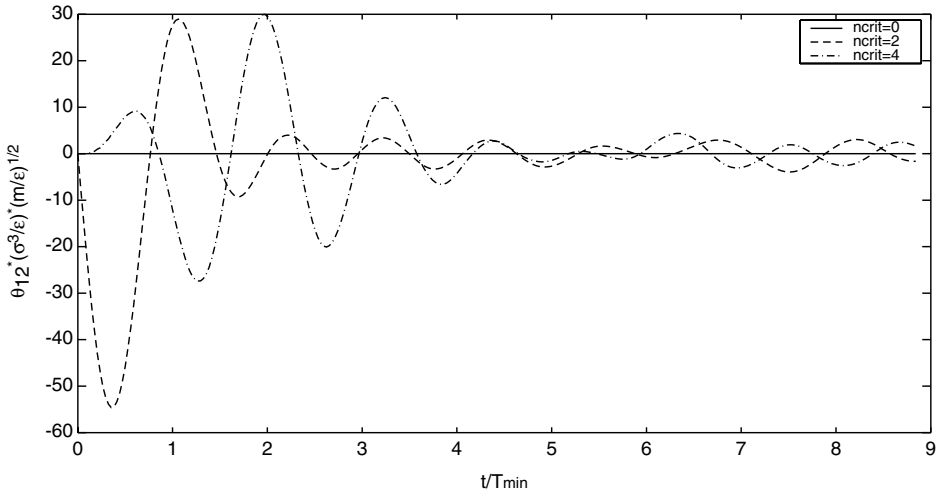

Figure 4. $\boldsymbol{\theta}_{12}(t)$ for zero and higher orders.

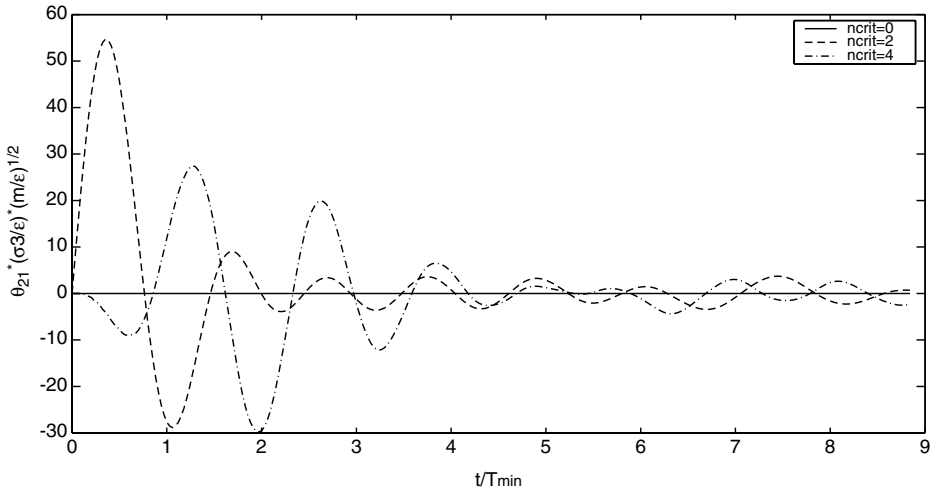

Figure 5. $\boldsymbol{\theta}_{21}(t)$ for zero and higher orders. Note that $\boldsymbol{\theta}_{21}(t) = -\boldsymbol{\theta}_{12}(t)$.

Furthermore, the higher order components are not only smaller in amplitude but are time delayed with respect to the zeroth-order. This makes sense, as the response of a neighbouring atomic unit cell to the perturbation of the boundary unit cell will be slower the further away the unit cells are. It is thus expected in numerical computation that the single biggest improvement will occur simply by utilizing the zeroth-order component of the time history kernel; as more neighbours are used, the solution should improve, but slowly and less dramatically.

(vi) An important point that will be exploited in our numerical simulations is the decaying nature of all of the components of the time history kernels. Because the long time values of the kernels are essentially inconsequential with regards to the short time values, it is expected that the kernels will

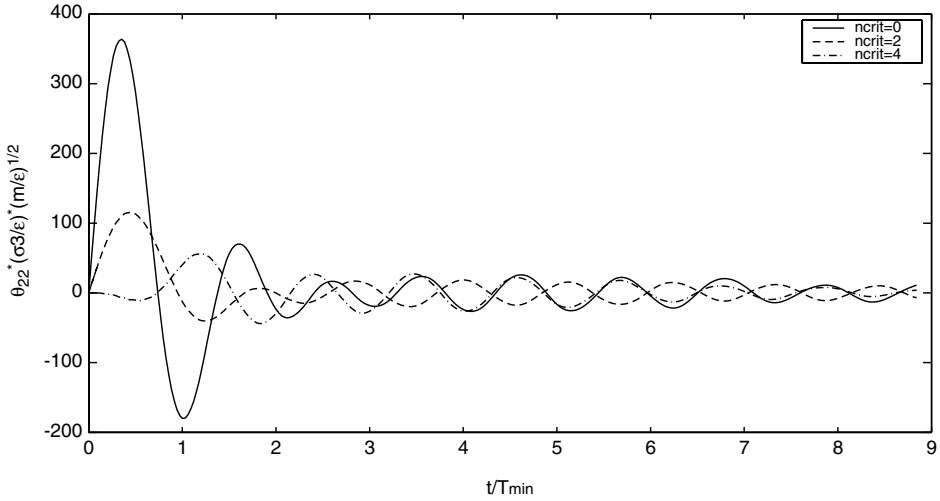

Figure 6. $\boldsymbol{\theta}_{22}(t)$ for zero and higher orders.

in practice be able to be truncated without significant loss in accuracy and with significant gains in computational efficiency.

(vii) We note that the time axes in figures 3–6 are normalized by the shortest period of vibration $T_{\min}$, corresponding to the longitudinal mode with wave vector $\mathbf{k} = \{0, 2\pi/\sqrt{3}a_0\}$ in a two-dimensional hexagonal lattice (see figure 2) with the LJ potential. In the expression for the wave vector $\mathbf{k}$, a_0 corresponds to the lattice parameter. It is noteworthy that the time history kernels are able to be truncated after less than ten atomic vibrational periods, and indicates that the time history dependence of the lattice does indeed decay quite rapidly.

2.4. *Aspects of numerical implementation: impedance force*

The numerical implementation of the MD impedance force (45) involves two components. The first component deals with the calculation of the time history kernel $\boldsymbol{\theta}(t)$. In practice, $\boldsymbol{\theta}(t)$ is computed and stored before the actual calculation takes place. The values of $\boldsymbol{\theta}(t)$ depend on the type of lattice considered, the interatomic potential utilized, and the number of atomic neighbours considered in calculating the impedance force. The interatomic potential influences the values of the stiffness matrix $\mathbf{K}$, for example in (33). In the numerical implementation, because of the decreasing nature of the time history kernel $\boldsymbol{\theta}(t)$, all components of $\boldsymbol{\theta}(t)$ are set to zero after a certain time, i.e. nine atomic vibrations corresponding to normalized time $t = 3$ in figures 3–6, which dramatically reduces the storage requirements for $\boldsymbol{\theta}(t)$.

A particular point of emphasis is that $\boldsymbol{\theta}(t)$ is *not* stored for every boundary atom. Because of the repetitive structure assumption used in deriving $\boldsymbol{\theta}(t)$, all boundary atoms in a given row can be considered to be identical. Therefore, only one set of $\boldsymbol{\theta}(t)$ is necessary, and is reused for each boundary atom. The number of $\boldsymbol{\theta}(t)$ stored then only depends on the number of atomic neighbours (n_{crit} in (45)) considered for each boundary atom.

Thus, the only variables that are required for the impedance force which require updating during the simulation is the difference in boundary displacements, or the $\mathbf{q}_{0,m'}(\tau) - \bar{\mathbf{u}}_{0,m'}(\tau)$ term in (45). This difference in displacement is stored for every boundary atom. The $\mathbf{q}_{0,m'}(\tau)$ term, or the displacements of each boundary atom, are available each MD time step. The $\bar{\mathbf{u}}_{0,m'}(\tau)$ term, or the interpolated FE displacement at each boundary atom, is calculated after each FE time step. Because that term is also necessary at each MD time step, it is integrated in time at each MD time step assuming a constant coarse scale acceleration and thus the difference $\mathbf{q}_{0,m'}(\tau) - \bar{\mathbf{u}}_{0,m'}(\tau)$ can be evaluated and stored for each MD time step. Details on the integration algorithm for both the coarse and fine scales can be found in Wagner and Liu (2003), and Park and Liu (2004).

Because the time history kernel $\boldsymbol{\theta}(t)$ is truncated after a certain period of time, the requirements for the displacement history are correspondingly truncated to hold for the same number of time steps. A further truncation on the storage of the displacement histories can be accomplished by only storing the displacement histories at certain time steps, while weighting those values accordingly to account for the fact that the displacement histories are not stored at every MD time step (Karpov *et al.*, 2005).

2.5. *Aspects of numerical implementation: coupling force*

We now discuss implementation-specific details of the coarse scale internal force in (46), i.e. the $\mathbf{N}^{\mathrm{T}}\mathbf{f}(\mathbf{u})$ term. This term originates naturally due to the separation of scales in constructing the multi-scale Lagrangian (6). In two dimensions, the size of the matrix $\mathbf{N}^{\mathrm{T}}$ is $N_{n1} \times N_{a1}$, where N_{n1} is the number of finite element nodes whose support contains an atomic position, and N_{a1} is the total number of atoms. The matrix $\mathbf{N}^{\mathrm{T}}$ is calculated once at the outset of the simulation as follows. First, a search is performed to determine which atoms lie within the interior of each finite element. The finite element shape functions are then evaluated at each initial atomic position which lies within the finite element. Because each node has a compact support, the matrix $\mathbf{N}^{\mathrm{T}}$ is stored as a sparse matrix. The x and y components of the finite element nodal forces can then be calculated as

$$f_{Ix} = \sum_{\alpha=1}^{n^I_{\mathrm{atom}}} N_I(\mathbf{X}_\alpha) f_{\alpha x}(\mathbf{u}), \tag{47}$$

$$f_{Iy} = \sum_{\alpha=1}^{n^I_{\mathrm{atom}}} N_I(\mathbf{X}_\alpha) f_{\alpha y}(\mathbf{u}), \tag{48}$$

where $N_I(\mathbf{X}_\alpha)$ are the finite element shape functions evaluated at the initial atomic positions $\mathbf{X}_\alpha$, f_{Ix} are the x components of finite element nodal forces, f_{Iy} are the y components of the finite element nodal forces, $f_{\alpha x}(\mathbf{u})$ are the x components of the standard MD interatomic forces evaluated as a function of the total displacements $\mathbf{u}$, $f_{\alpha y}(\mathbf{u})$ are the y components of the standard MD interatomic forces evaluated as a function of the total displacements $\mathbf{u}$ and n^I_{atom} are the number of atoms within the support of node I.

Equations (47) and (48) represent the discrete version of the coarse scale internal force derived consistently through the multi-scale Lagrangian in (6). It is important to note that for the case in which the finite element nodal positions exactly overlay

the atomic lattice, the coarse scale internal forces (47) and (48) will *exactly* correspond to the actual atomistic internal forces due to the Kronecker-delta property of the finite element shape functions. For the more general case in which the finite element nodal positions are spaced wider than the atomic lattice spacing, the coarse scale internal forces represent an average of the underlying atomic forces, with the quality of the approximation given by the finite element shape functions.

Due to the long-ranged interactions inherent in atomistic simulations, many situations will arise in which some portion of the force on a given atom will contain the effects of the motion of other atoms in different finite elements. However, because the force on each atom in (47) and (48) is a *total* value, no special treatment is needed to treat atomic bonds which cross finite element boundaries.

The coarse scale internal force for the N_{c2} nodes in region 2 is calculated in a different manner, due to the absence of atoms in that region. This is described in the following section.

2.6. *Cauchy–Born rule for coarse scale*

In the coarse scale-only region, where the MD force is unavailable (i.e. region 2 in figure 1), an approximation to the right-hand side of (46), the $\mathbf{N}^{\mathrm{T}}\mathbf{f}(\mathbf{u})$ term, must be made. Because of the desire to use the same interatomic potential to derive the finite element forces even in the absence of the underlying MD region, we use the Cauchy–Born rule in the region which contains only the coarse scale. We note that the Cauchy–Born rule is not the only possible method to represent the coarse scale internal force; other methods which do not require a hyperelastic stress update and only depend on the interatomic potential have been developed (Qian *et al.* 2004, Qian and Gondhalekar 2004). Due to the inherent limitations in the Cauchy–Born rule in describing the mechanics of carbon nanotubes, among other interesting structures, this ensures that the bridging scale is not correspondingly limited in this manner. Further details on the Cauchy–Born implementation for the bridging scale can be found in Wagner and Liu (2003), and Park and Liu (2004). Further details on the Cauchy–Born rule can be found in Tadmor *et al.* (1996).

2.7. *Staggered time integration algorithm*

As was previously mentioned, one strength of the bridging scale lies in the ability to update the MD and FE equations of motion using appropriate time steps for each equation. In fact, both simulations are integrated through time using widely utilized algorithms; velocity verlet for MD, and explicit central difference for FE. Details on the staggered time integration can be found in Wagner and Liu (2003) and Park and Liu (2004).

§ 3. Numerical examples

All MD calculations presented in this section utilize the LJ 6–12 potential, which takes the form

$$\Phi(r_{ij}) = 4\epsilon\left(\left(\frac{\sigma}{r_{ij}}\right)^{12} - \left(\frac{\sigma}{r_{ij}}\right)^{6}\right), \tag{49}$$

where σ has dimensions of length, ϵ has dimensions of energy and r_{ij} is the distance between two atoms i and j. The examples were run with parameter values $\sigma = \epsilon = 1$ considering nearest-neighbour interactions only, while all atomic masses were chosen

as $m = 1$. The interatomic distance r_{ij} which minimizes the potential energy Φ in (49) can be determined to be $2^{1/6}\sigma$.

A hexagonal lattice structure corresponding to the (111) plane of an fcc crystal was considered for the MD simulations, with the atoms initially in an equilibrium configuration. Because of the symmetry between the top and bottom layers of a hexagonal lattice, the time history kernels for the top and bottom layers can be related by

$$\boldsymbol{\theta}_n^{\text{top}}(t) = \boldsymbol{\theta}_{-n}^{\text{bottom}}(t), \tag{50}$$

and the storage requirements for the time history kernels can be reduced by one half. A schematic demonstrating the atomic directions along which the impedance force (45) was applied for all numerical bridging scale examples is shown in figure 7. In (50), $\boldsymbol{\theta}^{\text{top}}(t)$ corresponds to the $[\bar{1}2\bar{1}0]$ direction of a hexagonal lattice while $\boldsymbol{\theta}^{\text{bottom}}(t)$ can then be found using the symmetry arguments in (50). Figures 3–6 show the time history kernel for an LJ 6–12 potential computed for $\boldsymbol{\theta}^{\text{bottom}}(t)$. All simulations were performed with the random terms $\mathbf{R}(t)$ in (44) and (45) set equal to zero, indicating a continuum region at zero temperature. All MD simulations were correspondingly run using a zero temperature approximation.

For the regions which satisfy a coarse scale-only description, the Cauchy–Born rule was utilized to calculate the coarse scale internal force as described above. The LJ 6–12 potential was used to describe the continuum strain energy density, such that the coarse scale internal force could be derived from the same interatomic potential that was used for the MD force calculations. All numerical examples utilized quadrilateral 4-node bilinear finite elements to discretize the continuum.

We comment here on the usage of a general interatomic potential with parameters which do not match those of any real material. These choices were made in the interest of generality, such that large classes of realistic physical systems could be simulated without concentrating on a specific material. Future work could, of course, use specific values for σ and ϵ to match the behaviour of a given material should a detailed study of a specific physical process be desired. Finally, the LJ potential was chosen to represent a model brittle material.

All units related to atomistic simulations in this section, such as velocity, position and time, are given in reduced units. It should be noted that because of the choices of mass, σ and ϵ as unity, all normalization factors end up as unity. Finally, all

Figure 7. Schematic illustration of the boundaries on which the MD impedance force (45) was applied for all numerical examples.

numerical examples shown in this work were performed using the general purpose simulation code Tahoe, which was developed at Sandia National Laboratories (Tahoe 2004).

3.1. *Two-dimensional wave propagation*

In this example, we demonstrate the effectiveness of the bridging scale in eliminating high-frequency wave reflection between the FE and MD regions. To do so, a two-dimensional wave propagation example was run. A part of the MD region was given an initial displacement corresponding to a two-dimensional circular-type wave. The components of the initial displacements given in polar coordinates were

$$\mathbf{u}_r(r) = \frac{A}{A - u_c}\left(1 + b\cos\left(\frac{2\pi r}{H}\right)\right)\left(A\,\mathrm{e}^{-(r/\sigma)^2} - u_c\right)\hat{\mathbf{e}}_r. \tag{51}$$

The corresponding parameters had values of $\sigma = 15$, $H = \sigma/4$, $A = 0.015$, $b = 0.1$, $r_c = 5\sigma$ and $u_c = A\,\mathrm{e}^{(-r_c/\sigma)^2}$. A controls the wave amplitude, b controls the degree of high-frequency content in the wave ($b = 0$ implies zero high-frequency content) and r_c controls the cut-off distance of the initial displacements. The initial configuration for the problem is shown in figure 8.

In order to have a comparison for the bridging scale simulations, a larger MD simulation was performed, and taken to be the benchmark solution. In

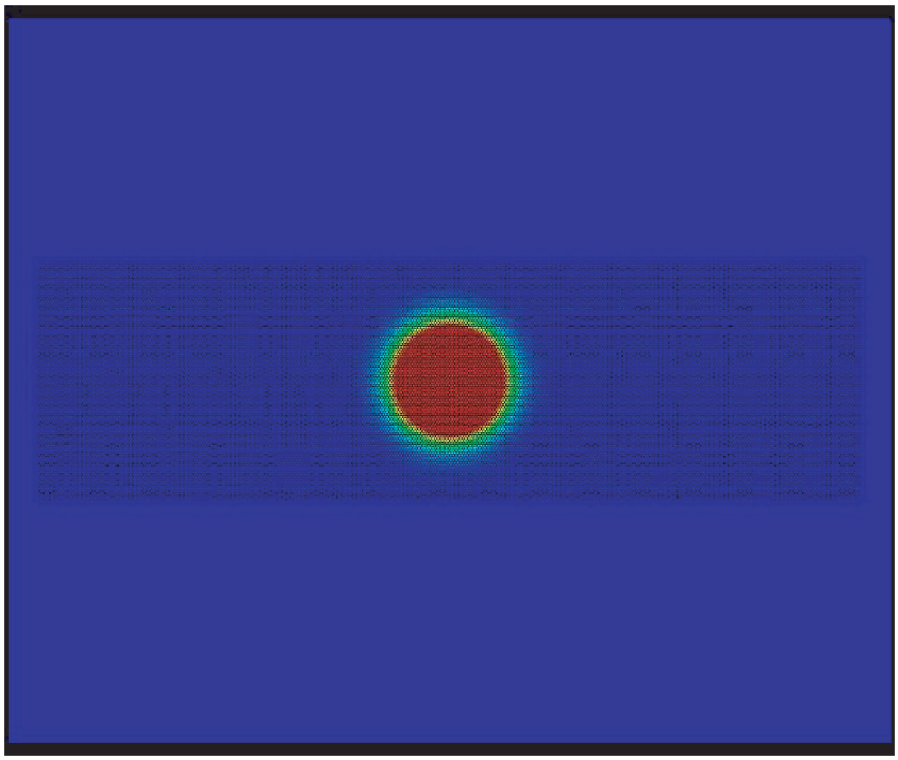

Figure 8. Initial conditions for two-dimensional wave propagation example. Contours of displacement magnitude shown.

this simulation, the same initial displacements prescribed by (51) for the bridging scale simulation were prescribed for the MD lattice. For the full MD region to match the entire bridging scale region, 91 657 atoms, or 301 atoms in the x direction along with 301 atoms in the y direction were used. The wave was allowed to propagate away from the centre of the lattice until just before the domain boundaries were reached.

The corresponding bridging scale simulation contained 31 157 atoms (301 atoms in the x direction by 101 atoms in the y direction) and 1920 finite elements, of which 600 were in the coupled MD/FE region. Twenty MD time steps were used for each FE time step. The bridging scale MD domain contained as many atoms in the x direction as the full MD simulation, but only one-third the number of atoms in the y direction. Because the MD boundary conditions were only enforced on the top and bottom atomic layers of the bridging scale MD lattice, this would ensure that the waves reached and passed through the top and bottom boundaries before the left and right boundaries were reached by the wave.

In order to test the accuracy of the MD impedance force, five cases were run. The first case involved not applying the impedance force, which would expectedly lead to large amounts of high-frequency wave reflection at the MD/FE boundary. Then, four cases were run in which the number of neighbours used in calculating the impedance force (n_{crit} in (45)) was increased. A snapshot showing the natural propagation of the wave which originated in the MD region into the surrounding continuum is shown in figure 9. It is important to note that while the continuum representation exists everywhere, that part of the FE mesh overlaying the MD region

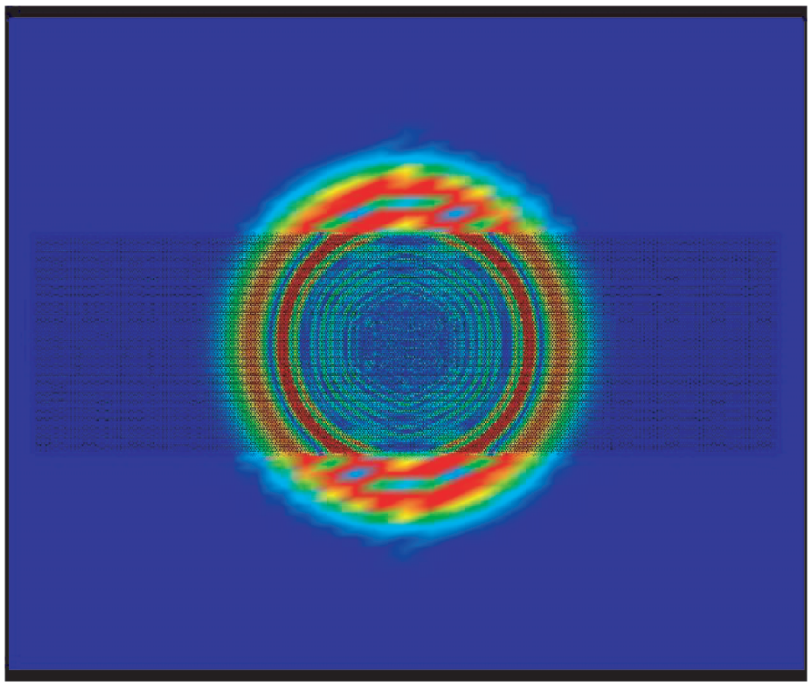

Figure 9. A later snapshot of wave propagation from the MD region into the continuum region. Contours of displacement magnitude shown.

is not shown to better illustrate how the coarse scale captures the information originating in the MD region.

The resulting total energy (kinetic energy+potential energy) transferred from the MD region using the bridging scale is shown in figure 10. The full MD energy was measured only in the region in which the bridging scale MD existed, such that a valid comparison could be made. The full MD energy was then normalized to be the reference solution, such that it tends to zero in figure 10. Of course, because the wave has not fully exited the system, the actual energy in all systems does not go to zero, but this normalization is performed such that a percentage measurement and comparison between the full MD and bridging scale MD systems can be obtained.

As figure 10 shows, if the MD impedance force (45) is not applied, only about 35% of the MD energy is transferred in comparison to the full MD. However, if the impedance force that is presented in this work is utilized, even if only one neighbour is used in calculating the boundary force (i.e. $n_{\text{crit}} = 0$), about 91% of the MD energy is transferred in comparison to the full MD simulation. The percentage steadily increases until more than 95% of the energy is transferred if nine neighbours ($n_{\text{crit}} = 4$) are used to calculate the impedance force. These results show the necessity in correctly accounting for the eliminated fine scale degrees of freedom in the form of the impedance force (45). The time axis of figure 10 has been normalized by t_{trans}, which represents the transit time that the shortest wavelength the FE mesh can support takes to reach the MD boundary from the

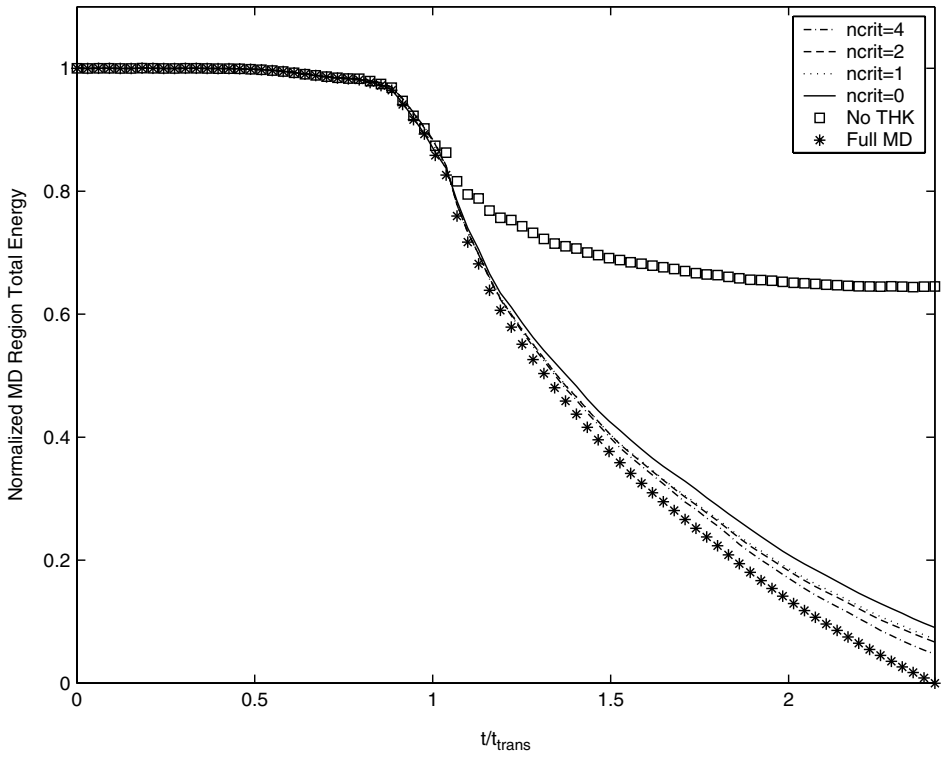

Figure 10. Comparison of energy transfer for two-dimensional wave propagation example.

centre of the MD region. As could be expected, energy begins to dissipate from the MD region around the normalized time of one.

A final note of importance is made in further analysing the bridging scale result shown in figures 11, 12. One element of the bridging scale simulation that results is a long wavelength reflection back into the MD region. The reason for this long wavelength reflection is due to the fact that the FE internal force is calculated by two different means for the boundary nodes. The result of this is a system with slightly different stiffnesses. For the problem shown in this section, because most of the initial MD energy is concentrated in the high-frequency waves, the majority of the energy is transferred into the continuum. In general, this may not be the case, and more of the system energy may be concentrated in the longer wavelengths.

There are multiple ways of reducing this effect. One approach is to split the boundary element such that it receives a contribution from both the MD forces and the Cauchy–Born forces. By doing so, a transition element is created whose properties are an average of the two systems. By creating this transition element, the long wavelength reflection is eliminated, as has been done in one-dimensional problems (Wagner and Liu 2003).

Another option is to use meshfree shape functions everywhere in the domain. Because of the non-local nature of the meshfree shape functions, the transition element described above will be naturally created without the need for special integration techniques for the boundary element. This issue will be addressed more carefully in a later work.

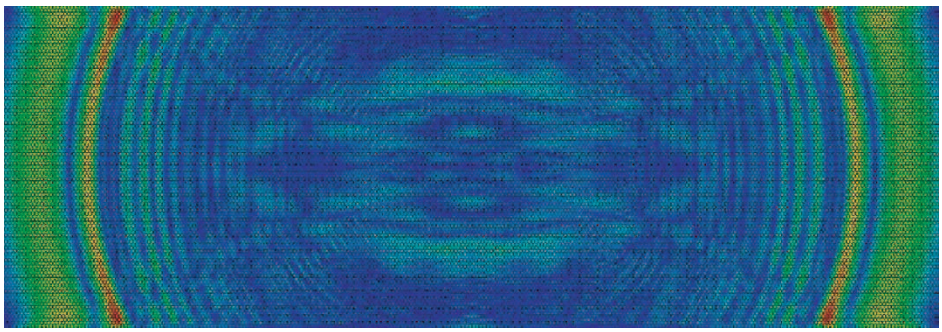

Figure 11. Final displacements in MD region if MD impedance force (45) is applied. Reprinted from Liu *et al.* (2004) with permission from the publisher.

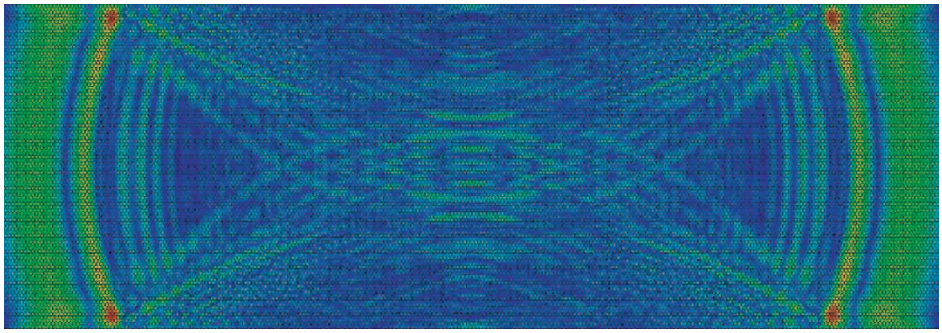

Figure 12. Final displacements in MD region if MD impedance force (45) is not applied. Reprinted from Liu *et al.* (2004) with permission from the publisher.

3.2. *Dynamic crack propagation in two dimensions*

The previous example dealt with a specific case in which all of the initial energy of the problem was in the MD domain and then dissipated away into the surrounding continuum. This type of example, while useful for verifying the effectiveness of the derived MD impedance force (45), does not demonstrate all relevant facets of a generalized multiple scale simulation. In fact, it could be reasonably argued that for problems such as the wave propagation example in which the only goal is to allow passage of the fine scale waves out of the MD region without causing internal reflection, using techniques such as those introduced by Wagner *et al.* (2004) and Karpov *et al.* (2005) would be sufficient, thereby rendering the coarse scale redundant.

However, many problems of interest involve those in which the MD region is not initially in a state of motion, and instead moves as a result of some initial continuum deformation which is passed to the MD region via the coarse scale/fine scale coupling established in (45). Because of this, it is important that the MD boundary condition acts as a two-way filter; first, that it allows large scale continuum information into the MD region. Secondly, that it still dissipates away the high-frequency MD waves which cannot be represented by the surrounding continuum. To demonstrate the truly two-way coarse/fine coupled nature of the bridging scale, we solve a two-dimensional dynamic crack propagation in which the boundary conditions are applied to the coarse scale. The problem schematic is shown in figure 13.

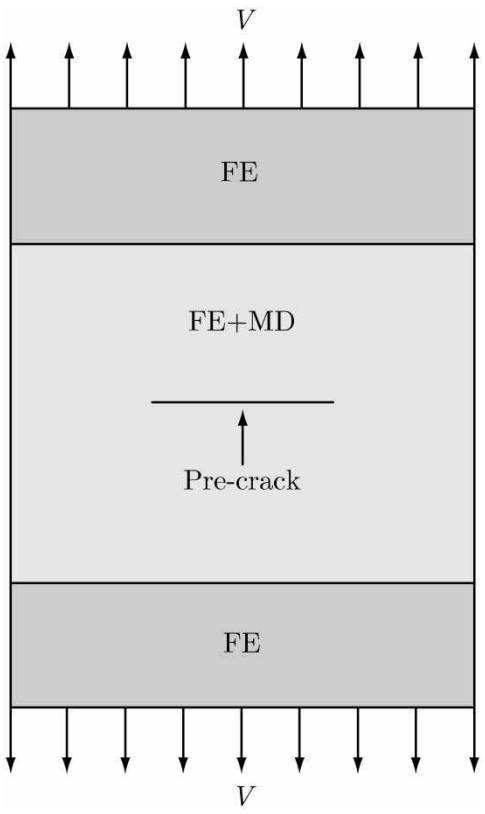

Figure 13. Configuration for two-dimensional dynamic crack propagation example.

The pre-crack is generated by preventing the interaction of two rows of atoms. In this way, the atoms on the faces of the pre-crack effectively behave as if on a free surface, and the crack opens naturally in tension. A ramp velocity is applied to the top and bottom nodes of the continuum region such that the atomistic fracture occurs in a mode-I fashion. The application of the ramp velocity is shown in figure 14.

A full MD simulation was also run in which the entire domain was comprised of atoms. The bridging scale simulation consisted of 91 051 atoms and 1800 finite elements, of which 900 were in the coupled MD/FE region. Forty MD time steps were run for each FEM time step. Correspondingly, the full MD simulation consisted of 181 201 atoms. The identical velocity boundary condition as shown in figure 14 was applied on the full MD simulation as was the bridging scale simulation, with the peak velocity $V_{\max} = 0.04$. For all bridging scale simulations shown in this section, only one neighbour was utilized in evaluating the impedance force, i.e. $n_{\text{crit}} = 0$.

A comparison between the full MD simulation and bridging scale simulations is shown in figures 15 and 16. In these figures, the potential energy of the MD domain is shown. As can be seen, both simulations show the same dominant characteristics, notably the size and intensity of the process zone immediately ahead of the crack tip, and also in the high-frequency radiation emitted from the crack tip. This high-frequency radiation, which appears as concentric circles radiating away from the crack tip, is emitted each time a single atomic bond is broken by the propagating crack. The opening of the crack is shown clearly by magnifying the y component of the displacement by a factor of 3. It should be noted that while the interatomic interactions have been restricted to nearest neighbours, the potential is not truncated at any point such that the potential energy and force are fully continuous functions of interatomic distance.

If a larger peak velocity $V_{\max}$ is chosen for the velocity boundary condition or the simulation is run for a sufficiently lengthy period of time, then complete

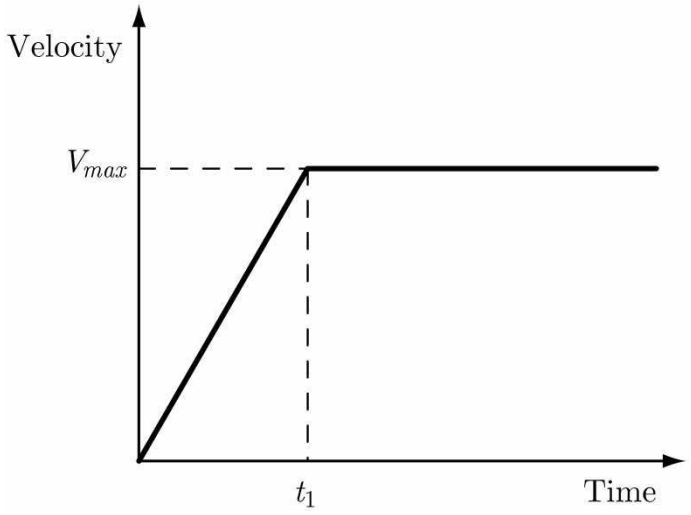

Figure 14. Ramp velocity boundary condition that is applied on FE region for dynamic fracture examples.

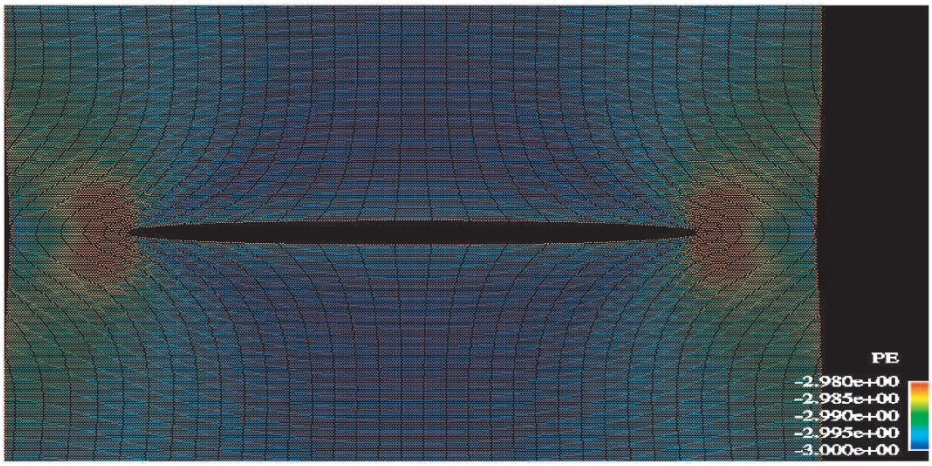

Figure 15. Potential energy contours of full MD fracture simulation.

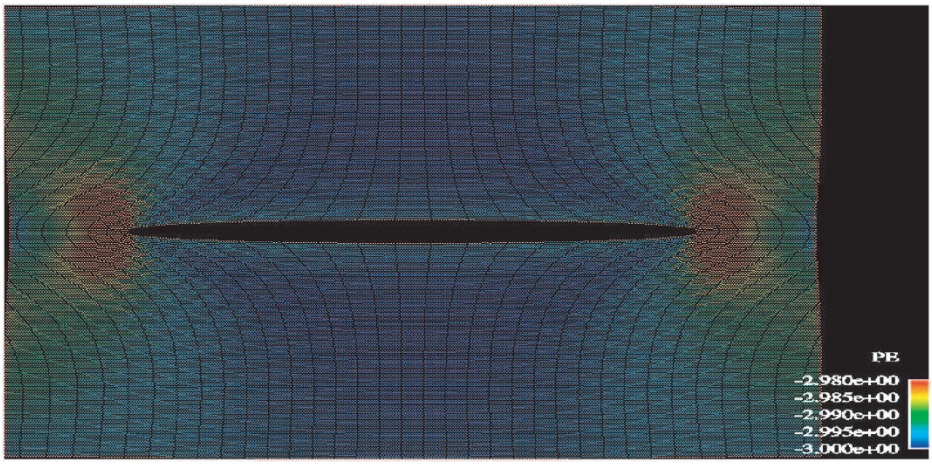

Figure 16. Potential energy contours of bridging scale fracture simulation.

fracture of the atomic lattice into two sections will occur. This is demonstrated in figures 17 and 18, where the peak velocity was chosen as $V_{\max} = 0.06$. As can be seen in figures 17 and 18, the bridging scale simulation agrees very well with the full MD simulation. It is also noteworthy that complete fracture of the underlying MD lattice is allowed in the coupled simulation; this is because the finite element nodal forces in that region are obtained directly from the underlying atomistic forces via (47) and (48). Because of this fact, no calculation of deformation gradients in the coupled MD/FE region is necessary. Therefore, the finite elements which overlay the MD region can deform in a manner that finite elements governed by traditional constitutive laws cannot. This is exemplified by the pinched nature of the deformation of the finite elements at the edge of the cracked specimen in figure 19, which shows the deformed FE mesh and separated MD lattice plotted together. Again, the crack opening is shown in the figures by magnifying the y component of the displacement by a factor of 3.

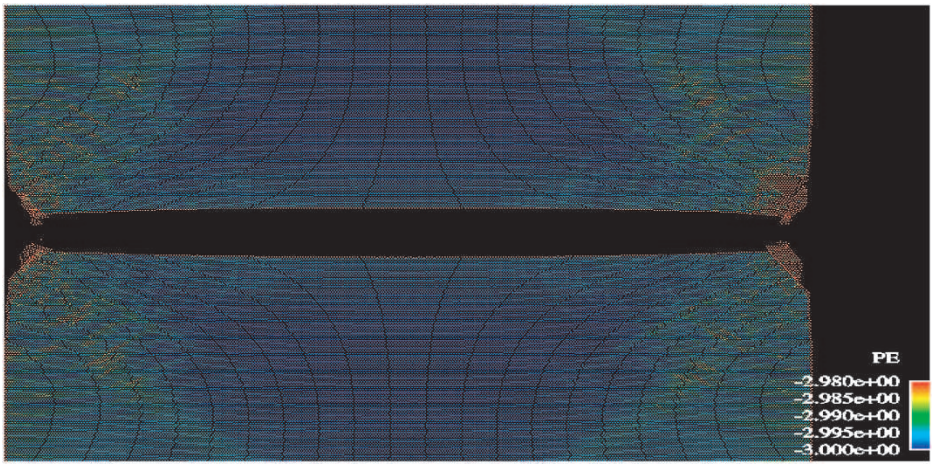

Figure 17. Potential energy contours of full MD simulation after complete fracture of lattice has occurred.

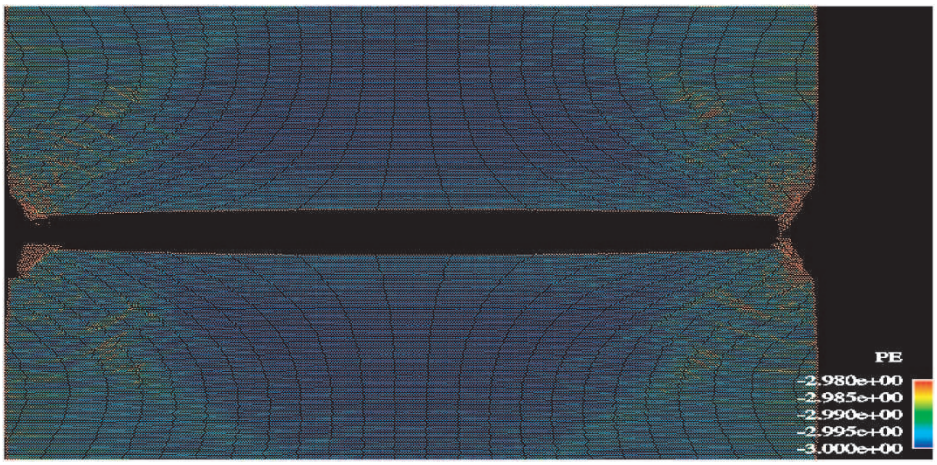

Figure 18. Potential energy contours of bridging scale simulation after complete fracture of lattice has occurred.

Another useful measure of comparison between the bridging scale and a full MD simulation is in tracking the initiation times and subsequent positions of the crack tips. In our simulations, because the location of the pre-crack is known, the location of the crack tip could be easily ascertained by comparing the y displacements of the atoms ahead of the pre-crack, and checking if they had exceeded a critical value. The comparison between the full MD and two different bridging scale simulations using different MD domain sizes is shown in figure 20, for the case $V_{\max} = 0.04$. As can be seen, the bridging scale simulations predict the identical crack initiation time as the full MD simulation as well as the position of the crack tip as it evolves through time.

A slightly different system was run for further comparisons. In this case, the full MD system contained 362 101 atoms (601 atoms in the x direction by 601

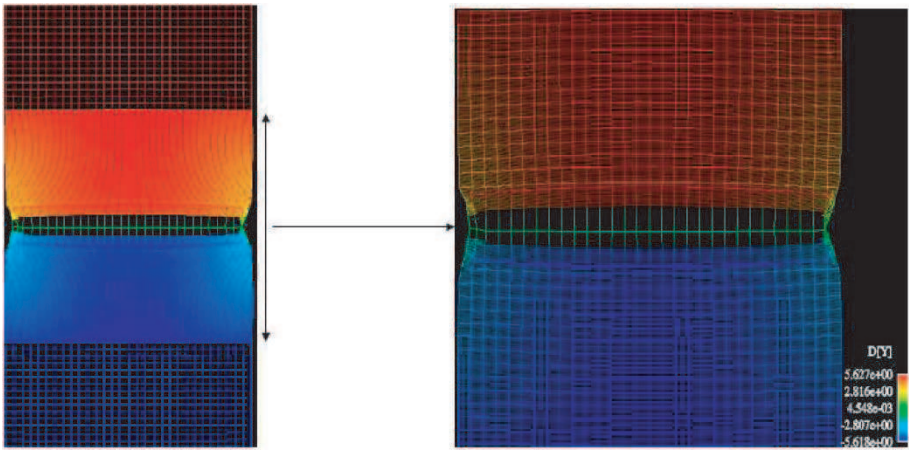

Figure 19. Left: y displacements of entire structure. Note that MD exists only in a small part of the domain, while FE exists everywhere. Right: zoom in of y displacements in coupled MD/FE region. Reprinted from Liu *et al.* (2004) with permission from the publisher.

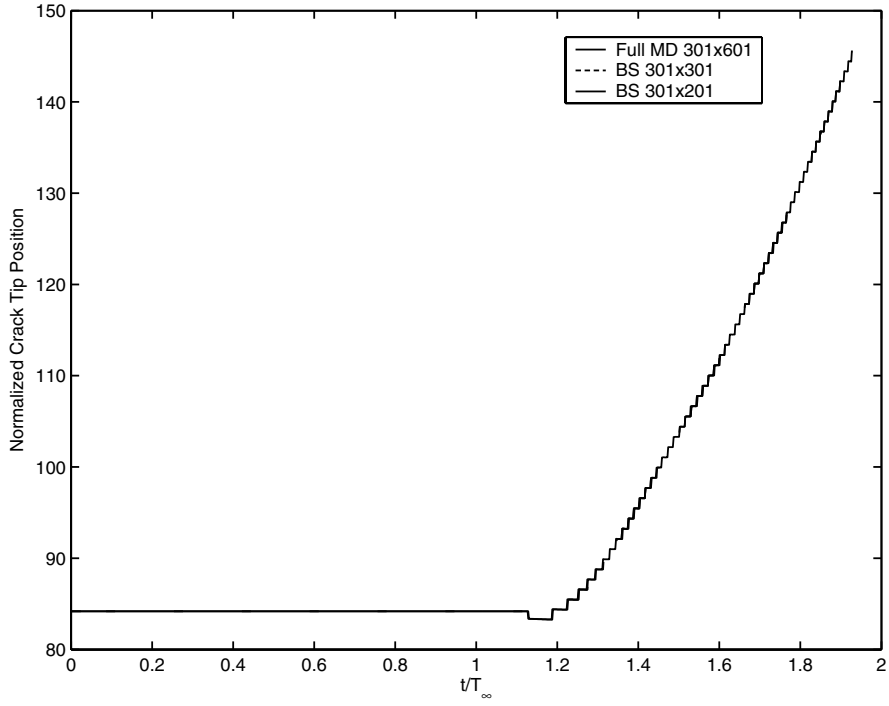

Figure 20. Comparison of crack position with respect to time for full MD and two different bridging scale simulations.

atoms in the y direction). Three different bridging scale simulations with varying MD system sizes (601×301, 601×201, 601×101) along with 3600 finite elements were run. The crack tip history is shown in figure 21. As can be seen, the first two bridging scale simulations match the crack initiation time and time history exactly. However, for the smallest MD region within a bridging scale simulation (the 601×101 atom case),

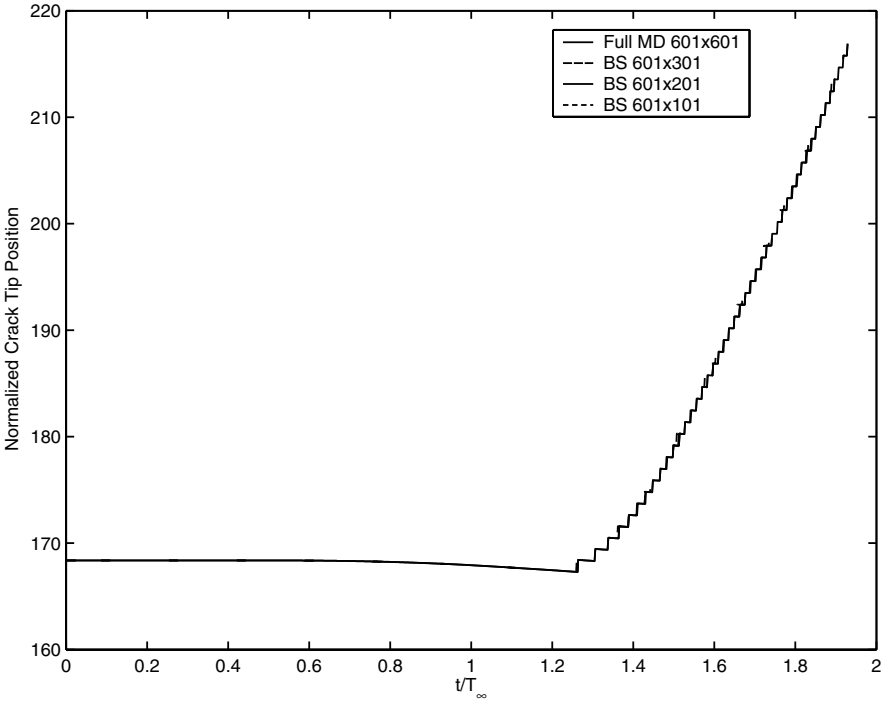

Figure 21. Comparison of crack position with respect to time for full MD and three different bridging scale simulations.

the crack initiates at a slightly earlier time than in the full MD case. After initiation, the velocity of the crack appears to match the velocity of the crack in the full MD case. We note that other simulations were run in which the number of atoms in the y direction was reduced to less than 101. For these simulations, the crack either initiated much earlier or later than expected, or did not initiate at all. It appears as though the incorrect physics demonstrated in this case reflects the assumption of linearity at the MD boundary being violated if the MD region is too small.

Taken together, figures 20 and 21 demonstrate the truly two-way coupled nature of the derived MD boundary condition (45). Firstly, the large scale information which is passed to the MD region as a boundary condition is being passed correctly; this is borne out by the fact that the crack initiation times in the bridging scale simulations match the initiation times in the full MD simulations. Secondly, the derived MD boundary condition effectively dissipates high-frequency waves emitted from the crack tip; this is revealed by the fact that the position of the crack tip over the entire duration of propagation matches that of the full MD simulation. More simply, the high-frequency waves emitted by the crack tip are not reflecting from the MD boundary and interfering with the crack propagation dynamics.

The time axis in figures 20 and 21 was normalized by a critical time T_∞ corresponding to the time that a crack in an infinite strip would begin initiation under mode-I type loading, where the crack driving force under plane stress is given to be

$$G = \frac{E\delta^2}{2h(1-\nu^2)}. \tag{52}$$

Simulation	Normalized Time
Full MD: 362101 atoms = 724202 DOF's	1.0
Bridging Scale: 121901 atoms + 3721 nodes = 251244 DOF's	0.51
Bridging Scale: 61851 atoms + 3721 nodes = 131144 DOF's	0.33

Figure 22. Comparison of simulation times using bridging scale vs. full MD. $n_{\text{crit}} = 0$ for bridging scale simulations.

In (52) G is the crack driving force, E is the Young's modulus, ν is Poisson's ratio, δ is the applied displacement to the strip edge and h is the total height of the strip. Along the cleavage plane created in the simulation, extending the crack by a distance of the lattice parameter a_0 requires the breaking of two bonds. Therefore, the fracture energy is $2\epsilon/a_0$. For both the full MD system as well as the bridging scale calculations, crack initiation occurred later than predicted by the analytical relations, indicating that the specimen considered is not sufficiently long in the x direction for (52) to hold.

Finally, a comparison of the computational expense incurred utilizing the bridging scale versus a pure atomistic simulation is shown in figure 22. The full MD simulation of 362 101 atoms was set as the benchmark simulation in terms of computational time. This benchmark full MD simulation was then compared to two bridging scale simulations. The first used approximately one-third the number of atoms, 121 901, along with 3721 FE nodes. The second used approximately one-sixth the number of atoms, 61 851, along with 3721 FE nodes. As can be seen, computational speedups of two and three times were observed, respectively, using the bridging scale for the case in which all computations were performed in serial. The bridging scale simulation times do not scale exactly as the fraction of MD degrees of freedom due to the additional expense of the terms introduced by the bridging scale coupling, and also because certain optimization tools, such as the truncation of the number of displacement histories stored per boundary atom as done in Park and Liu (2004) and Karpov *et al.* (2005), have not yet been implemented.

§ 4. Conclusions

The major thrust of this work has been to present the fundamentals necessary to make the bridging scale, a method designed to couple atomistic and continuum simulations, valid for simulations in multiple dimensions. The key step has been in developing a technique to numerically calculate the time history kernel matrix $\boldsymbol{\theta}(t)$, which mimics the dissipation of high-frequency fine scale waves into the eliminated fine scale degrees of freedom, in multiple dimensions. Similar to the single scale work by Wagner *et al.* (2004) and Karpov *et al.* (2005), a multiple scale method for numerically accounting for the eliminated fine scale degrees of freedom in the form of an impedance force that acts upon the reduced MD

lattice was presented. The major assumptions of the method include a planar MD boundary, approximating the interatomic forces of the eliminated MD degrees of freedom as a linear function of atomic displacements, and a repetitive, crystalline lattice structure. Incorporating this methodology into the bridging scale framework leads to a truly two-way coupled boundary condition on the MD simulation, which allows the dissipation of high-frequency waves into the surrounding continuum while also passing long wavelengths from the continuum into the atomistic region.

The numerical examples presented in this work illustrate two important concepts. The wave propagation examples demonstrated that the numerically calculated time history kernel $\boldsymbol{\theta}(t)$ acts to eliminate high-frequency waves that cannot be represented by the continuum. The dynamic crack propagation example demonstrated the truly two-way nature of the MD impedance force; boundary conditions applied to the continuum caused the atomistic crack to grow, while the MD impedance force containing $\boldsymbol{\theta}(t)$ again removed high-frequency waves emitted by the propagating crack which cannot be represented by the continuum.

In comparing the bridging scale to other multi-scale methods, the following conclusions can objectively be drawn. First, due to the existence of a clearly delineated coarse and fine scale, the coarse scale time step is not restricted to the stable MD time step. Because the coarse scale is not required to update at the same time scales as the MD simulation, an enormous computational savings is achieved compared to those methods that require a one-to-one atom to node mesh. Another major advantage of the bridging scale lies in the mathematically consistent treatment of the removed fine scale degrees of freedom. Because those removed fine scale degrees of freedom contribute to the MD equation of motion through the MD impedance force, it is exactly clear why the method succeeds in the elimination of high-frequency waves leaving the atomistic region; the wave propagation example shown in this work conclusively demonstrates the importance of correctly accounting for the removed fine scale degrees of freedom.

The form of the time history kernel matrix $\boldsymbol{\theta}(t)$ also constitutes one of the major advantages of the bridging scale. It was shown that, unlike previous methods, $\boldsymbol{\theta}(t)$ is a compact matrix, whose size corresponds to the minimum number of degrees of freedom in each unit cell. Furthermore, a simple numerical procedure to calculate $\boldsymbol{\theta}(t)$ was discussed, which utilizes only standard Laplace and Fourier transform techniques. Lastly, the geometry of the lattice structure need not be explicitly modelled; all geometric effects are implicitly included in the lattice stiffness, or $\mathbf{K}$ matrices. We close the summary of the bridging scale by noting that it is valid for dynamic, finite-temperature problems.

Future work on the bridging scale can be decomposed into three major tasks. The first task is to extend the method to allow fully coupled finite-temperature simulations. Due to the presence of the random terms $\mathbf{R}(t)$, the continuum is allowed to exert thermally motivated forces on the atomistic region. While there is no restriction on the temperature of the atomistic region, there is currently no established manner in which the internal energy generated within the MD region is passed or represented accurately in the continuum. Further research is needed to develop a heat conduction equation for the coarse scale which can accurately represent the energy dissipated from the MD region due to the impedance force.

The second crucial future task involves the relaxation of the fact that only nearest-neighbour atomic interactions were considered in this paper. As stated

within this article, this is not a restriction on the method itself; the derivation for the time history kernel $\boldsymbol{\theta}(t)$ can be extended to including non-nearest-neighbour interactions simply by utilizing a larger unit cell, which would allow the usage of longer-ranged potentials such as the embedded atom method (EAM) (Daw and Baskes 1984). This generalisation has indeed been performed, and the results of this investigation will be reported in Park *et al.* (2004).

A third goal is to relax the small displacement assumption that exists in calculating the time history kernels $\boldsymbol{\theta}(t)$. In principle, because the impedance force (45) represents a zeroth-order linearization of the interatomic forces, higher order terms could be used to represent moderate nonlinearities and rotations at the MD boundary.

One final note of importance concerns the issue of time scale with respect to the MD simulation. While the expense of the MD simulations in this work was cut by reducing the size of the MD domain, the issue of extending the time scales that can be simulated using MD still remains, and is beyond the scope of this work. It may be possible in the future to use methods such as that of Voter *et al.* (2002) to extend the time scales that are currently available within a standard MD simulation. However, these methods are currently valid only for infrequent event simulations, such as diffusion, and may not be applicable to the problems presented in this work.

Acknowledgements

We would like to thank the National Science Foundation (NSF) and the NSF-IGERT program for their support. We would also like to thank the NSF Summer Institute on Nano Mechanics and Materials and the Army Research Office (ARO) for supporting this work. HSP expresses his grateful thanks to the Engineering Sciences Summer Institute (ESSI) at Sandia National Laboratories. Sandia National Laboratories is supported by the U.S. Department of Energy under contract DE-AC04-94AL85000. The authors would like to acknowledge Dr. Gregory Wagner, Dr. Hiroshi Kadowaki and Professor Ted Belytschko for their kind assistance and helpful discussions on the bridging scale, and also Dr. Jonathan Zimmerman for his guidance and discussion on the dynamic fracture problem. Finally, we would like to thank Dr. Thao D. Nguyen for sharing her insights into dynamic fracture analysis.

APPENDIX A

§A1. *Derivation of stiffness matrices*

We derive here the details related to the usage of the time history kernel $\boldsymbol{\theta}(t)$. A crucial component in determining $\boldsymbol{\theta}(t)$ lies in the stiffness matrices $\mathbf{K}$, as in (20). We first define a unit cell n, m, as shown in figure A1, and the other cells interacting with n, m.

In general, the $\mathbf{K}$ matrices can be defined as

$$\mathbf{K}_{n-n',m-m'} = \frac{\partial \mathbf{f}_{n,m}}{\partial \mathbf{r}_{n',m'}}(\mathbf{r} = \mathbf{r}_{\mathrm{e}}), \tag{A1}$$

where $\mathbf{r}$ is a vector of current atomic positions in the repetitive cell and $\mathbf{r}_{\mathrm{e}}$ denotes the vector of corresponding equilibrium positions. For the LJ 6–12 potential utilized throughout this work, the $\mathbf{K}$ matrices are found as functions of an interaction coeffi-

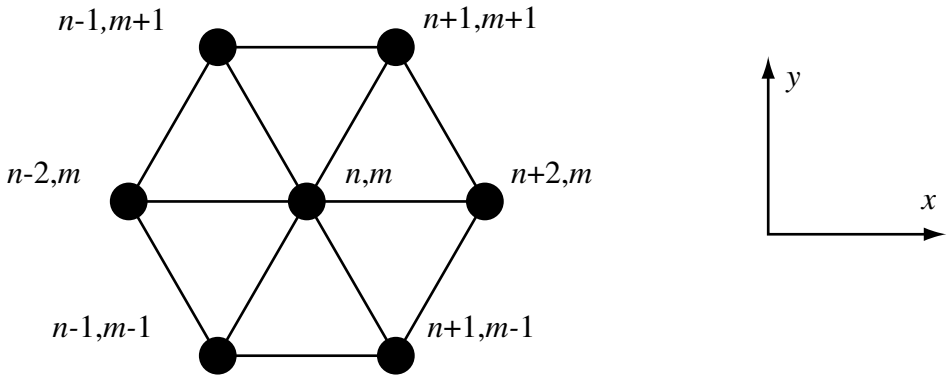

Figure A1. Basic unit cell n, m with neighbouring (interacting) unit cells.

cient k, where k is defined to be

$$k = \frac{\partial^2 \Phi(r)}{\partial r^2}(r = r_e), \tag{A2}$$

and r is a scalar representing the distance between two atoms. Utilizing the above definition, it is found that

$$k = 36(4)^{1/3}\frac{\epsilon}{\sigma^2}. \tag{A3}$$

Furthermore, the scalar distance r_e which minimizes the potential energy of the LJ potential can be determined to be

$$r_e = 2^{1/6}\sigma. \tag{A4}$$

For a given lattice structure and coordinate system, the interaction coefficient k defined in (54) defines all **K** matrices uniquely. The **K** matrices are now given as

$$\mathbf{K}_{1,1} = \mathbf{K}_{-1,-1} = \frac{k}{4}\begin{pmatrix} 1 & \sqrt{3} \\ \sqrt{3} & 3 \end{pmatrix}, \tag{A5}$$

$$\mathbf{K}_{-1,1} = \mathbf{K}_{1,-1} = \frac{k}{4}\begin{pmatrix} 1 & -\sqrt{3} \\ -\sqrt{3} & 3 \end{pmatrix}, \tag{A6}$$

$$\mathbf{K}_{2,0} = \mathbf{K}_{-2,0} = k\begin{pmatrix} 1 & 0 \\ 0 & 0 \end{pmatrix}, \tag{A7}$$

$$\mathbf{K}_{0,0} = k\begin{pmatrix} -3 & 0 \\ 0 & -3 \end{pmatrix}. \tag{A8}$$

APPENDIX B

§B1. *Discrete Fourier transform*

The discrete Fourier transform (DFT) is used to transform functions from real space to wavenumber space. Assuming that the function f can be defined at all

atomic positions l, we denote the value of f and position l as f_l. The DFT of f, which is described using the hatted notation, is defined to be

$$\hat{f}(p) = \mathcal{F}_{l\to p}\{f_l\} \equiv \sum_{l=-(L/2)+1}^{L/2} f_l \, \mathrm{e}^{-i2\pi pl/L}, \tag{B1}$$

where L denotes the number of lattice sites, and p can take any integer value between $-(L/2)+1$ and $L/2$. The inverse Fourier transform (IFT) is then defined to be

$$f_l = \mathcal{F}^{-1}_{p\to l}\{\hat{f}(p)\} \equiv \frac{1}{L} \sum_{p=-(L/2)+1}^{L/2} \hat{f}(p) \, \mathrm{e}^{i2\pi pl/L}. \tag{B2}$$

We close by noting the convolution property of the DFT, i.e. that the transform of the convolution of two functions in space is equal to the product of the transforms of the individual functions

$$\mathcal{F}_{l\to p}\left(\sum_{l'=-(L/2)+1}^{L/2} f_{l-l'} g_{l'} \right) = \hat{f}(p)\hat{g}(p). \tag{B3}$$

§B2. *Laplace transform*

The Laplace transform (LT) is used to transform functions of time t into the transformed variable s. The LT of a function $f(t)$ is defined to be

$$F(s) = \mathcal{L}\{f(t)\} \equiv \int_0^\infty f(t) \, \mathrm{e}^{-st} \, \mathrm{d}t. \tag{B4}$$

The inverse Laplace transform (ILT) is defined to be

$$f(t) = \mathcal{L}^{-1}\{F(s)\} \equiv \frac{1}{2\pi i} \int_{c-i\infty}^{c+i\infty} F(s) \, \mathrm{e}^{st} \, \mathrm{d}s, \tag{B5}$$

where c is a constant greater than the real parts of all singularities of $F(s)$. We give two other important definitions for the LT, first the transform of the time derivative of a function

$$\mathcal{L}\left\{ \frac{\mathrm{d}^n f(t)}{\mathrm{d}t^n} \right\} = s^n F(s) - s^{n-1} f(0) - s^{n-2} \frac{\mathrm{d}f}{\mathrm{d}t}(0) - \cdots - \frac{\mathrm{d}^{n-1} f}{\mathrm{d}t^{n-1}}(0). \tag{B6}$$

Finally, similar to the DFT, the LT of a convolution integral of two functions is equal to the product of the transforms of the individual functions

$$\mathcal{L}\left\{ \int_0^t f(t-\tau) g(\tau) \, \mathrm{d}\tau \right\} = F(s)G(s). \tag{B7}$$

References

Abraham, F. F., Broughton, J., Bernstein, N., and Kaxiras, E., 1998, *Europhys. Lett.*, **44**, 783.

Adelman, S. A., and Doll, J. D., 1976, *J. chem. Phys.*, **64**, 2375.

Cai, W., DeKoning, M., Bulatov, V. V., and Yip, S., 2000, *Phys. Rev. Lett.*, **85**, 3213.

Curtin, W. A., and Miller, R. E., 2003, *Model. Simul. mater. Sci. Engng*, **11**, R33.

Daw, M. S., and Baskes, M. L., 1984, *Phys. Rev.* B, **29**, 6443.

E, W., and Huang, Z. Y., 2002, *J. comput. Phys.*, **182**, 234.
Kadowaki, H., and Liu, W. K., 2004, *Comput. Methods appl. Mech. Engng*, **193**, 3267.
Karpov, E. G., Stephen, N. G., and Dorofeev, D. L., 2002, *Int. J. Solids Struct.*, **39**, 4291.
Karpov, E. G., Stephen, N. G., and Liu, W. K., 2003, *Int. J. Solids Struct.*, **40**, 5371.
Karpov, E. G., Wagner, G. J., and Liu, W. K., 2005, *Int. J. numer. Methods Engng* (accepted).
Liu, W. K., Karpov, E. G., Zhang, S., and Park, H. S., 2004, *Comput. Methods appl. Mech. Engng*, **193**, 1529.
Liu, W. K., Uras, R., and Chen, Y., 1997, *J. appl. Mech.*, **64**, 861.
Park, H. S., and Liu, W. K., 2004, *Comput. Methods appl. Mech. Engng*, **193**, 1733.
Park, H. S., Karpov, E. G., and Liu, W. K., 2004a, *Comput. Methods appl. Mech. Engng*, **193**, 1713; 2004b, *Int. J. numer. Methods Engng*, submitted.
Qian, D., and Gondhalekar, R. H., 2004, *Int. J. multiscale comput. Engng*, in press.
Qian, D., Wagner, G. J., and Liu, W. K., 2004, *Comput. Methods appl. Mech. Engng*, **193**, 1603.
Rudd, R. E., and Broughton, J. Q., 1998, *Phys. Rev.* B, **58**, 5893.
Shilkrot, L. E., Miller, R. E., and Curtin, W. A., 2004, *J. Mech. Phys. Solids*, **52**, 755.
Tadmor, E., Ortiz, M., and Phillips, R., 1996, *Phil. Mag.* A, **73**, 1529.
Tahoe, 2004, Sandia National Laboratories: http://tahoe.ca.sandia.gov.
Voter, A. F., Montalenti, F., and Germann, T. C., 2002, *A. Rev. Mater. Res.*, **32**, 321.
Wagner, G. J., and Liu, W. K., 2001, *Int. J. numer. Methods Engng*, **50**, 507; 2003, *J. comput. Phys.*, **190**, 249.
Wagner, G. J., Karpov, E. G., and Liu, W. K., 2004, *Comput. Methods appl. Mech. Engng*, **193**, 1579.
Xiao, S., and Belytschko, T., 2004, *Comput. Methods appl. Mech. Engng*, **190**, 1645.
Zhang, L. T., Wagner, G. J., and Liu, W. K., 2002, *J. comput. Phys.*, **176**, 483.